A finite volume Chimera method for fast transient dynamics in compressible flow problems

Alexis Picard, Nicolas Lelong, Olivier Jamond, Vincent Faucher, Christian Tenaud

A Finite Volume Chimera Method for Fast Transient Dynamics in Compressible Flow Problems

Alexis Picard[a,b], Nicolas Lelong[a], Olivier Jamond[a], Vincent Faucher[c], Christian Tenaud[d]

[a] *Université Paris-Saclay, CEA, Service d'Études Mécaniques et Thermiques, 91191, Gif-sur-Yvette, France.*
[b] *Université Paris-Saclay, CNRS, LISN, 91400, Orsay, France.*
[c] *CEA, DES, IRESNE, DTN, Cadarache, F-13108 Saint-Paul-Lez-Durance, France.*
[d] *Université Paris-Saclay, CNRS, Centrale Supélec, Laboratoire EM2C, 91190, Gif-sur-Yvette, France.*

Abstract

This article deals with fast transient dynamics of compressible flows in which local flow details matter. An overlapping grid Chimera method is proposed in a finite volume framework. Euler's equations are considered, as well as explicit time integration with a second order discretization in time and space. The method is intended to improve the accuracy of a large scale calculation by adding a local grid containing important flow details that alter the flow within the global grid. This paper evaluates the impact of the Chimera exchange on flow dynamics crossing the overlapping grid interface. The proposed Chimera method is assessed using five well-known test cases from the literature. With a second order interpolated solution inside the receiving cells, the method does not alter the order of convergence of the global model. It is able to deal with complex compressible flow structures as well as multi-component flows, and produces numerical solutions with better quality when using a finer local model compared to a single grid computation, providing significant gains in terms of CPU time and memory usage.

Keywords: Chimera method, Overlapping grids, Fast transient dynamics, Finite volume, Compressible flow, Two-phase flow

1. Introduction

Studying accidental situations involving highly pressurized systems or explosive transients in large and complex geometries is of importance for safety issues in industrial environments. For instance, such accidental situations can be found in the nuclear framework when Loss of Primary Coolant Accidents [1] or H2 explosions [2] occur. The brutal accidental context implies compressible flow features such as discontinuities (shock waves, rarefaction fans or contact discontinuities) or acoustic waves travelling and interacting at high speeds. Moreover, interactions between these waves possibly produce vortical structures through baroclinic effect, mainly if multi-phasic or multi-component mixtures are at play. Fast transient energetic flows may also finally interfere with deformable structures inducing coupled phenomena at very small time scales ($10^{-6} - 10^{-3} s$ [3]). Due to the risks and the general difficulty to perform tests with fully representative geometry and initial conditions in the range described above, numerical simulation appears as a powerful and convenient way to characterize the response of the systems during such transients. Producing accurate and reliable results in these configurations however represents a challenging task since the computational domain must account simulaneously for the largest

scale of the geometry and for small geometrical details inducing local flow patterns with significant influence on the global solution. Dealing with all the scales within one mesh classically yields huge numbers of grid points and complex meshing procedures. One elegant alternative is then to associate, within one composite simulation independent numerical models, in terms of both geometry and mesh, each adapted to the physical phenomena of interest at different time and space scales.

The present work intends to provide a numerical strategy which consists in introducing some localized geometrical alterations or details in a large scale global numerical model involving multicomponent flows. As a particular attention is paid to the conservativity of the numerical scheme, the proposed approach falls within the framework of the finite volume method. In addition, in readiness for an industrial usage, this strategy should offer a high flexibility and user-friendliness. In particular, the large scale grid should be kept unmodified. To this end, the proposed approach relies on the introduction of the considered alteration in a local grid which is overlaid with the global one. To ease the generation of this local model, it is meshed independently from the mesh of the global model. Also, it can be meshed finer than the global grid to increase the accuracy of the solution near the introduced alteration.

Such a localized increase of accuracy can be achieved using a patch based Adaptive Mesh Refinement (AMR) approach [4]. However, the AMR approach is not straightforward to introduce a localized alteration of the geometry in the large scale numerical model and does not provide the flexibility of using non-matching grids. Then the proposed approach does not involves AMR, whereas it could certainly be used in a complementary way. The first overlapping grid method that we are interested in is the so-called Arlequin method that has been introduced by H. Ben Dhia [5]. It has been applied to a large panel of problems, mainly structural [6, 7, 8, 9], but also to some compressible fluid mechanics problems [10, 11, 12]. The present work also benefits from the previous work carried out by Fernier *et al.* [13], in which the relevance of the Arlequin method for structural fast transient dynamic simulation with explicit-explicit time integration is demonstrated. However, the Arlequin method shows some limitations with fluid fast transient dynamics in [14] with the appearance of ghost forces, numerical artifacts that require a filtering procedure. Also, it has been designed for a finite element framework and thus would require a conversion to our framework as, to the best of our knowledge, the Arlequin method has not been used in a finite volume context.

The second method considered is the Chimera method developed by Steger and Benek [15] and further extended in [16] and [17]. The main idea of the Chimera method is to allow independent and non-matching grids to transfer information using existing cells or nodes as a receiving container. Like the Arlequin method, the Chimera method requires an overlapping zone for the information to be transferred. It also presents the same flexibility but has been designed for a finite difference framework and has been translated to a finite volume framework. The Chimera method has been extensively reviewed with a finite difference framework for compressible turbulent flows [18, 19, 20, 21, 22] mostly for aircraft applications [23, 24, 25, 26] but also wave propagation [27], incompressible flows [28, 29] and inviscid compressible flows [30, 31]. In each case, the Chimera method provides with a good solution for overlapping grids apart from introducing an interpolation error which can be compensated by using a higher order interpolation for the exchange procedure than the order of the numerical scheme. More recently, the Chimera method has been transposed to a finite volume framework and has been tested for various aircraft applications with compressible turbulent flows and implicit time integration [32, 33]. The Chimera method has also been used with inviscid compressible flows in [34] where the time integration is implicit as they are not dealing with fast transient dynamic and in [35, 36], where

the Chimera method is combined with AMR for reactive flows. The Chimera method has also been tested with remeshing techniques like in [37, 38] but this type of method is out of scope as we do not want to alter the global grid. Several references can be found on the use of a Chimera method combined with moving Cartesian grids [34], [39] for rotor computations or complex aircraft geometries [40]. In this paper, we are not interested in moving grids as we want to assess the impact of an overlapping grid technique on the numerical solution of the flow. In other words, we are focusing on applications in which a geometrical detail contained inside a local grid generates flow structures that cross the overlapping grid interface and improve the global grid solution. Recently, high-order Chimera methods have been developed in [41] with global to local frame transformations and in [42, 43] with a Moving Least Square reconstruction technique. The method has also been coupled with Arbitrary Lagrangian Eulerian (ALE) formulations in a finite element context in [44] which show its compatibility with FSI.

In most of the previously cited applications, the Chimera method is used to patch a geometrical detail that drives the dynamics of the flow [39, 36]. In this paper, the flow dynamics is initially generated outside the patched grid, in a large domain. The patch is used to take into account a geometrical detail that significantly alters the flow dynamics over a large scale domain. The patch is attached to a geometrical detail that is stationary. Therefore, the flow dynamics must go through the overlapping grid interface without distortion. A Chimera method is used to transfert information between overlapping grids. The first novelty of this paper is that the interpolation of the transferred information is based on a local conservation hypothesis with a second order reconstruction instead of a polynomial reconstruction [34, 43]. The reconstructed solution is limited using a modified finite volume limiter. The second novelty of this paper is that a particular attention is paid to the impact of the Chimera method on the flow dynamics crossing the overlapping grid interface. We specifically focus on the impact of the Chimera method combined with variable cell ratios between the global grid and the finer local grids. The developed method is fully compatible with multi-phase/multi-component flows. Considering fast transient flows allows us to neglect viscous effects in relation to acoustic and wave propagation phenomena [45]. Euler's equations will be considered, as well as explicit time integration.

The paper is organized as follows. First, a description of the governing equations used in our context is given section § 2. After briefly introducing the numerical methods, we present our finite volume Chimera method, detailing the reasons for the approach and then the improvements needed to fulfil the requirements in section § 3. Section § 4 is dedicated to the assessment and the validation of the developed method on five well-known test cases in the literature, each one chosen to stress the method on one specific aspect, thus providing an overview of the method's capabilities and limitations. The last section gathers the main conclusions and prospects for future improvements of the method.

2. Governing Equations

The present study relates on fast transient dynamics phenomena. Therefore, we assume that the viscous effect could be neglected in favor of convection and acoustic transports [45], and we here consider the Euler system of equations. In the context of multi-component flows, the governing equations are based on the compressible version of the reduced five-equation two-phase flow model proposed by Allaire *et al.* [46], specially designed for interface problems. The five-equation model is applied to the Euler equations. The governing equations written in a vectorial form, express the conservation of mass, momentum and total energy for a two-fluid medium as follows:

$$\frac{\partial}{\partial t}(\mathbf{U}) + \nabla \cdot \mathbf{F}(\mathbf{U}) = \mathbf{B}(\mathbf{U})\, \nabla \cdot \mathbf{u}, \tag{1}$$

with the vector of independent variables ($\mathbf{U}$), the Euler fluxes ($\mathbf{F}(\mathbf{U})$), and the source terms ($\mathbf{B}(\mathbf{U})$) are the following:

$$\mathbf{U} = \begin{pmatrix} \rho_1\alpha_1 \\ \rho_2\alpha_2 \\ \rho\mathbf{u} \\ \rho E \\ \alpha_1 \end{pmatrix}, \quad \mathbf{F}(\mathbf{U}) = \begin{pmatrix} \rho_1\alpha_1\mathbf{u} \\ \rho_2\alpha_2\mathbf{u} \\ \rho\mathbf{u}\otimes\mathbf{u} + p\mathbf{I_d} \\ (\rho E + p)\mathbf{u} \\ \alpha_1\mathbf{u} \end{pmatrix} \quad \text{and,} \quad \mathbf{B}(\mathbf{U}) = \begin{pmatrix} 0 \\ 0 \\ 0 \\ 0 \\ \alpha_1 \end{pmatrix}, \tag{2}$$

where $\mathbf{I_d}$ stand for $d \times d$ identity matrix, where d is the space dimension. We also note $\mathbf{Q} = (\rho, u, v, w, p)^t$ the vector of primitive variables. In these equations, ρ is the density, p the pressure, $\mathbf{u} = (u, v, w)^t$ the velocity vector, and E the total energy per unit of mass of the two-fluid mixture. α_k is the volume fraction of the phase k. Thus for a two-component fluid, the following constraint has to be considered $\alpha_1 = 1 - \alpha_2$. ρ_k is the density of the phase k, and the density of the mixture (ρ) is defined as: $\rho = \rho_1\alpha_1 + \rho_2\alpha_2$. The two-component fluid is supposed to have the same velocity $\mathbf{u}$. An isobaric closure is chosen so that $p = p_1 = p_2$.

The pressure (p) is related to the conservative quantities through the perfect gas equation of state (EOS). In this context, each fluid k is characterized by its equation of state:

$$p = (\gamma_k - 1)\rho_k e_k, \tag{3}$$

where γ_k is the heat capacity ratio , and e_k is the internal energy relative to phase k. The speed of sound in the phase k is $c_k = \sqrt{\frac{\gamma_k p}{\rho_k}}$.

Regarding the mixture, the specific internal energy ($e = E - \|\mathbf{u}\|^2/2$) is defined as $\rho e = \rho_1\alpha_1 e_1 + \rho_2\alpha_2 e_2$. The speed of sound ($c$) associated to the mixture is defined in [46] by:

$$\rho\xi c^2 = \rho_1\alpha_1\xi_1 c_1^2 + \rho_2\alpha_2\xi_2 c_2^2, \tag{4}$$

with $\xi_k = \rho_k(\partial e_k/\partial p_k)$ and $\xi = \xi_1\alpha_1 + \xi_2\alpha_2$. In the following, this model is referred as to two-component model.

3. Numerical Methods

The integration of the system of equations 1 is based on an explicit finite volume method. Meshes are made of 2D polygonal control volumes $(K_i) \in \mathcal{U}$ extruded in the third direction, where $\mathcal{U}$, is the ensemble of control volumes belonging to the computational domain.

3.1. The second order TVD MUSCL scheme

We denote by $\Omega_{\mathcal{U}}$ the number of cells within the domain $\mathcal{U}$. We denote by $\gamma(i)$ the index set of cells neighboring K_i. For all cells $j \in \gamma(i)$, we define s_{ij} the common surface that separates K_i from K_j and $\mathbf{n}_{ij}$ the normal of s_{ij} directed from K_i to K_j. We write $|K_i|$ the volume of K_i and $|s_{ij}|$ the surface of the face s_{ij}. We introduce the discrete times: $\forall\ n \geq 0$, $t^{n+1} = t^n + \Delta t_n$ where Δt_n is the variable time step at the n-th time-step, which is subjected to a CFL condition. In the followings, we note $\mathbf{U}_i^n = \dfrac{1}{|K_i|}\displaystyle\int_{K_i} \mathbf{U}(\mathbf{x}, t^n)\, dx$ the numerical approximation at the cell K_i and at the time t^n, of the vector of conservative variables solution of equations 1. Let us notice that $\mathbf{Q}_i^n$ stands for the numerical approximation of the vector of primitive variables and $\mathbf{u}_i^n$ denotes the velocity vector of the cell K_i at the time t^n.

To obtain an approximate solution at a discrete time t^{n+1}, equation 1 is dicretized using a 2nd order (in time and space) Godunov type method based on the MUSCL reconstruction [47, 48, 49]. Regarding the non-conservative product, the term $\mathbf{B}(\mathbf{U})$ is approximated at the first order in time which leads to:

$$\mathbf{U}_i^{n+1} = \mathbf{U}_i^n - \frac{\Delta t_n}{|K_i|} \sum_{j\in\gamma(i)} \int_{s_{ij}} \mathbf{F}(\mathbf{U}^\star) \cdot \mathbf{n}_{ij}\, ds + \frac{\Delta t_n}{|K_i|} \mathbf{B}(\mathbf{U}_\mathbf{i}^\mathbf{n}) \sum_{j\in\gamma(i)} \int_{s_{ij}} \mathbf{u} \cdot \mathbf{n}_{ij}\, ds, \tag{5}$$

where $\mathbf{U}^\star$ is a solution of the Riemann problem depending on multiple cells. We introduce the numerical flux functions,

$$\hat{\mathbf{F}}\Big(\mathbf{U}^{\star\,n}_{ij}(\mathbf{U}_{ij}^n, \mathbf{U}_{ji}^n), \mathbf{n}_{ij}\Big) \approx \frac{1}{|s_{ij}|} \int_{s_{ij}} \mathbf{F}(\mathbf{U}^\star) \cdot \mathbf{n}_{ij}\, ds, \tag{6}$$

and

$$\hat{u}_{ij}\Big(\mathbf{U}^{\star\,n}_{ij}(\mathbf{U}_{ij}^n, \mathbf{U}_{ji}^n), \mathbf{n}_{ij}\Big) \approx \frac{1}{|s_{ij}|} \int_{s_{ij}} \mathbf{u}_i^n \cdot \mathbf{n}_{ij}\, ds, \tag{7}$$

whose purposes are to approximate the flux integral and the normal velocity, respectively, over the interface s_{ij}. The solution $\mathbf{U}^{\star\,n}_{ij}(\mathbf{U}_{ij}^n, \mathbf{U}_{ji}^n)$ is the approximated solution resulting from the Riemann problem at the interface s_{ij} [50], where the left and right states of the Riemann problem are given respectively by the interface states $\overline{\mathbf{U}}_{ij}^n$ and $\overline{\mathbf{U}}_{ji}^n$. Equation 5 can then be expressed using the Riemann interface state $(\mathbf{U}^{\star\,n}_{ij})$ as follows:

$$\mathbf{U}_i^{n+1} = \mathbf{U}_i^n - \frac{\Delta t_n}{|K_i|} \sum_{j\in\gamma(i)} |s_{ij}| \hat{\mathbf{F}}(\mathbf{U}^{\star\,n}_{ij}, \mathbf{n}_{ij}) + \frac{\Delta t_n}{|K_i|} \mathbf{B}(\mathbf{U}_\mathbf{i}^\mathbf{n}) \sum_{j\in\gamma(i)} |s_{ij}|\, \hat{u}_{ij}(\mathbf{U}^{\star\,n}_{ij}, \mathbf{n}_{ij}). \tag{8}$$

In the context of a 2nd order Godunov approach based on a MUSCL scheme [50], the interface states are reconstructed using a piecewise linear function of the primitive variables:

$$\overline{\mathbf{Q}}_{ij}^n = \mathbf{Q}_i^n + \Phi_i \nabla(\mathbf{Q}_i^n)(\mathbf{x}_{ij} - \mathbf{x}_i), \qquad \overline{\mathbf{Q}}_{ji}^n = \mathbf{Q}_j^n + \Phi_j \nabla(\mathbf{Q}_j^n)(\mathbf{x}_{ji} - \mathbf{x}_j), \tag{9}$$

where $\mathbf{x}_{ij}$ is the position of the interface center between two consecutive cells K_i and K_j, $\nabla(\mathbf{Q}_i^n)$ is the gradient of the solution $\mathbf{Q}_i^n$ expressed using primitive variables and Φ_i is the limiting function evaluated in the cell K_i also called limiter. The limiter employed in this work is the K-limiter of Dubois [51]. The gradient is constant in the cell and is approximated using a *Least squares method* [52]. The interface Riemann problem is solved using an approximate HLLC Riemann Solver presented in [50] and the normal velocity of the non-conservative term is computed using the HLLC solver for the advection equation detailed in [53]. The time integration scheme is a second order MUSCL-Hancock method which is combined with a second order TVD MUSCL scheme to give a second-order accurate method in both time and space [50].

3.2. The Chimera interpolation method

3.2.1. Method principle

The multi-model method that we have developed falls within the framework of the Chimera method [15, 16, 17]: It is a multi-model approach that allows overlapping grids to exchange information through a volumic exchange zone. These exchange zones are defined using cells that receive information, designated as ghost cells in the followings (see figure 1).

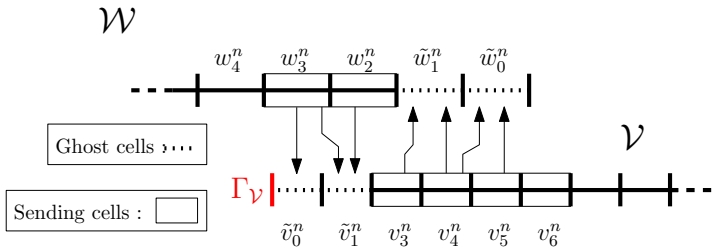

Figure 1: Sketch of the transfer procedure in the Chimera method.

We consider a baseline grid $\mathcal{W} = \{K_i\}_{i\in\Omega_{\mathcal{W}}}$ that is referred as substrate and a secondary grid $\mathcal{V} = \{K_i'\}_{i\in\Omega_{\mathcal{V}}}$ that is referred as patch. What we call *the substrate* refers to the global model while what we call *the patch* is a local model superimposed onto a part of the substrate. We note $\{\mathbf{w}_i\}_{i\in\Omega_{\mathcal{W}}}$, the conservative variables resolved on the substrate, $\{\mathbf{v}_i\}_{i\in\Omega_{\mathcal{V}}}$ the conservative variables resolved on the patch.

Our finite-volume Chimera method relies on the injection inside ghost cells of conservative variables interpolated using the corresponding neighbor cells on the other mesh, at every time step. The set of ghost cells are denoted $\widetilde{\mathcal{V}} \subset \mathcal{V}$ and $\widetilde{\mathcal{W}} \subset \mathcal{W}$. The interpolated solutions are written $\{\widetilde{\mathbf{w}}_i\}_{i\in\Omega_{\widetilde{\mathcal{W}}}}$ for the substrate and $\{\widetilde{\mathbf{v}}_i\}_{i\in\Omega_{\widetilde{\mathcal{V}}}}$ for the patch as represented in the figure 1. The sending cells are denoted $\mathcal{W}^s \subset \mathcal{W}$ and $\mathcal{V}^s \subset \mathcal{V}$ and are intersected by the ghost cell sets $\widetilde{\mathcal{V}}$ and $\widetilde{\mathcal{W}}$ respectively. Let us emphasize that the integration of the solution is performed everywhere except on the ghost cells that are only used for computing the numerical fluxes at sending cell interfaces. In other words, solution on ghost cells is only updated through the Chimera procedure at every time step. Let us also underline that the procedure is built as symmetrical, meaning that the way to transfer information from the patch to the substrate is identical as to transfer information from substrate to the patch.

Using the notation introduced in figure 1, we note $h_i^{\mathcal{V}}$ and $h_j^{\mathcal{W}}$, respectively, measures of the cells $K_i' \in \widetilde{\mathcal{V}}$ and $K_j \in \widetilde{\mathcal{W}}$. For each ghost cell from the patch K_i', $i \in \Omega_{\widetilde{\mathcal{V}}}$, we define the local

cell ratio between the patch and the substrate as :

$$\chi_i^{\mathcal{V}} = \max_{j \in \Omega_{K_i' \cap \mathcal{W}^s}} \left(\frac{h_j^{\mathcal{W}}}{h_i^{\mathcal{V}}}\right). \tag{10}$$

The equivalent definition can be made for a local cell ratio between the substrate and the patch and is the reciprocal of the previous definition. However, in our multi-model approach, we are interested in adding local models to the baseline model, thus the local cell ratio between the patch and the substrate is more adapted to our approach. We define the cell ratio χ as a global grid parameter for both models using the definition:

$$\chi = \max_{i \in \Omega_{\widetilde{\mathcal{V}}}} (\chi_i^{\mathcal{V}}). \tag{11}$$

The global definition makes sense in the case of regular grid spacing inside each model. Considering that the time integration of the numerical scheme is explicit, we have also chosen an explicit coupling between grids for the Chimera procedure [18, 35] as its implementation in an explicit time-integration context is straightforward.

3.2.2. Ghost cell detection and marking

Compared to the original and previous Chimera methods described in [18, 19, 54, 35, 36], we modified the ghost cell detection since we do not want to deactivate any cell nor modify grids. The proposed Chimera procedure is designed to be as flexible and independent as possible from the baseline simulation. The detection of ghost cells happens only once because the patch is considered fixed during calculation. We first prescribe a number of ghost cell layers (noted k_{GC}) required to calculate the numerical fluxes at interfaces of sending cells. We will see hereafter how to chose k_{GC}. Then, given the boundary $\Gamma_{\mathcal{V}}$ of the patch domain, the procedure identifies cells from the patch that will be marked as ghost cells $\widetilde{\mathcal{V}}$, as displayed in figure 2.

Once ghost cells $\widetilde{\mathcal{V}}$ are identified, the geometrical intersection $\widetilde{\mathcal{V}} \cap \mathcal{W}$ is calculated to mark the corresponding sending cells $\mathcal{W}^s$. Symetrically, $\widetilde{\mathcal{W}}$ is defined by searching the closest k_{GC} ghost cell layers to $\widetilde{\mathcal{V}}$ that respects the following condition for an explicit Chimera interpolation [18]:

$$\widetilde{\mathcal{W}} \cap \widetilde{\mathcal{V}} = \emptyset \text{ and } \widetilde{\mathcal{W}} \cap \mathcal{V} \neq \emptyset. \tag{12}$$

Similarly to the patch, once substrate ghost cells $\widetilde{\mathcal{W}}$ are identified, the intersection $\widetilde{\mathcal{W}} \cap \mathcal{V}$, is computed to mark the corresponding sending cells $\mathcal{V}^s$.

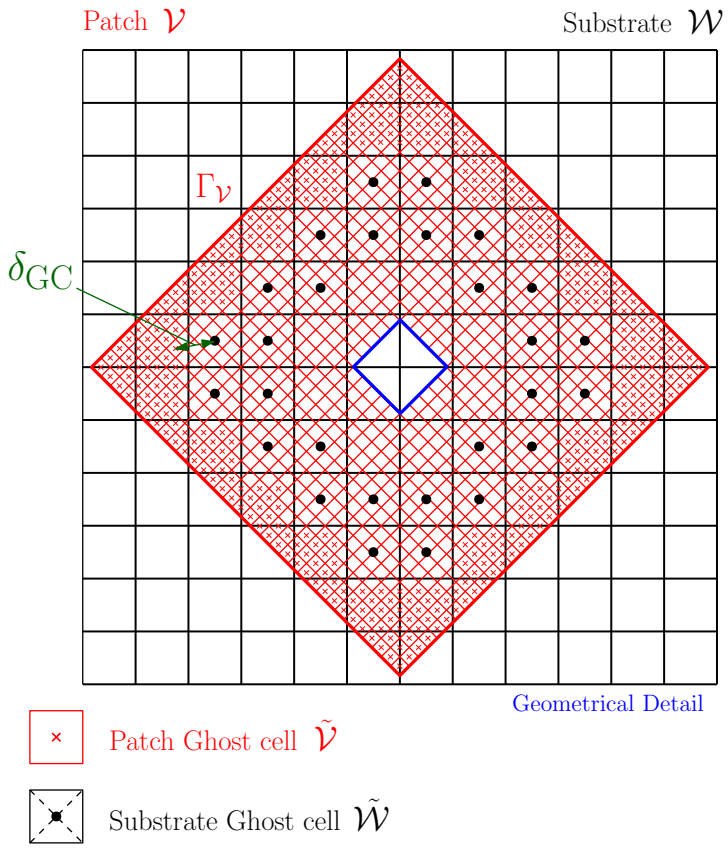

Figure 2: Ghost cell detection procedure for a 2nd order reconstruction ($N = 2$) with $\chi = 4$

As we are interested in the effect of χ within the framework of the Chimera exchange, we need to define the exchange zone gap as:

$$\delta_{\mathrm{GC}} = \min_{i \in \Omega_{\tilde{\mathcal{W}}}} \Big(\min_{j \in \Omega_{\tilde{\mathcal{V}}}} (|\mathbf{x}_j - \mathbf{x}_i|) \Big). \tag{13}$$

The final step of our ghost cell detection procedure consists in minimizing δ_{GC}, by potentially marking additional cells as ghost cells if they geometrically lie in between the ghost cell layers of the patch and the ghost cell layers of the substrate without breaking the condition 12. As a result, the ghost cell layers of the patch are extended to fit the ghost cell layers of the substrate. This step eventually improves the stability of the Chimera exchange when dealing with high cell ratio χ and complex flow structures.

3.2.3. Number of ghost cell layers

As we mentioned above, we need to prescribe a number of ghost layers (k_{GC}) before labeling the ghost cells. As mentioned in [55], a 2nd order accurate evaluation of the numerical flux at an interface between two consecutive cells needs a stencil over a neighborhood of two cells consecutive from each side of the interface. When a sending cell (either $\mathcal{W}^s$ or $\mathcal{V}^s$) is close to the boundary of the domain ($\Gamma_{\mathcal{W}}$ or $\Gamma_{\mathcal{V}}$, respectively), the number of ghost cells must be large enough

to ensure that the numerical flux evaluation does not intercept the boundary Γ. The situation is illustrated in a 1D sketch in figure 3. Regarding the interface $s_{i\,i-1}$, the numerical solution in cell K_i obtained through a second order finite-volume reconstruction imposes to keep a layer of two ghost cells to be independent of any boundary $\Gamma_{\mathcal{V}}$, as confirmed by [56] for an explicit interpolation. As values inside ghost cells are updated at each time step from the opposite model, the boundary condition at $\Gamma_{\mathcal{V}}$ has no impact on the solution in the sending cells. Reciprocally, cells that are not ghost cells that belong to the substrate portion covered by the patch has no impact on the solution inside the patch. In the followings, k_{GC} will always set to $k_{\text{GC}} = 2$.

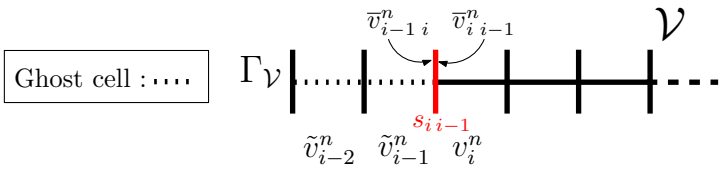

Figure 3: Chimera boundary condition.

3.2.4. A second order Chimera interpolation

As we are using a conservative finite-volume approach, the present Chimera method is based on local conservation hypothesis when transfer occurs between opposite grids. Indeed as it is shown in figure 4, the method relies on the intersection of ghost cells with the opposite grid.

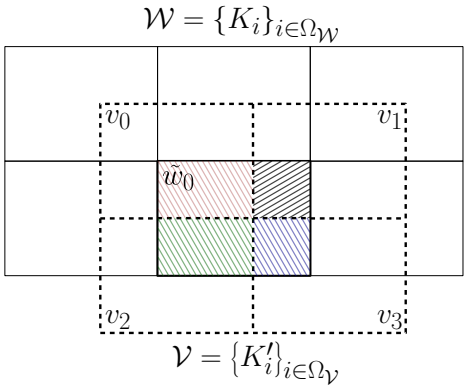

Figure 4: Example of a ghost cell intersection $\widetilde{K}_0$ with $\mathcal{V}$.

From a finite-volume framework, considering the ghost cell $\widetilde{K}_i$ in $\mathcal{W}$, we suppose that:

$$\int_{\widetilde{K}_i} \widetilde{\mathbf{w}}\, dV = \int_{\widetilde{K}_i \cap \mathcal{V}} \mathbf{v}\, dV. \tag{14}$$

Considering that the finite-volume numerical scheme is second order accurate in time and space, a piecewise linear reconstruction of the transferred solution is adequate to achieve the suitable accuracy order compared to a constant piecewise approximation of the solution.

Defining the barycenter position of the intersection $\widetilde{K}_i \cap K_j^{'}$ inside the ghost cell $\widetilde{K}_i$, noted $\widetilde{\mathbf{x}}_{ij}$, we can discretize equation 14 with a piecewise linear reconstruction: $\forall\ i \in \Omega_{\widetilde{\mathcal{W}}}$,

$$\widetilde{\mathbf{w}}_i^n = \sum_{j \in \Omega_{\mathcal{V}}} \frac{|\widetilde{K}_i \cap K_j^{'}|}{|\widetilde{K}_i|} \overline{\mathbf{v}}_j^n(\widetilde{\mathbf{x}}_{ij}) = \sum_{j \in \Omega_{\mathcal{V}}} \frac{|\widetilde{K}_i \cap K_j^{'}|}{|\widetilde{K}_i|} \Big(\mathbf{v}_j^n + \Phi_j \nabla(\mathbf{v}_j^n)(\widetilde{\mathbf{x}}_{ij} - \mathbf{x}_j) \Big), \tag{15}$$

where $\nabla(\mathbf{v}_j^n)$ is the gradient of the solution $\mathbf{v}_j^n$ based on conservative variables. The gradient is calculated for each sending cell set ($\mathcal{W}^s$ and $\mathcal{V}^s$) using a *Least squares method* [52]. Φ_j is the limiter also used for the gradient reconstruction 9 to evaluate the numerical flux. A slope limiter is employed to avoid spurious oscillation and so keeps the TVD property of the solution when transfer on the opposite model is performed. The present formulation ensures a spatial 2nd-order accurate interpolation in ghost cells without any constraint on meshes; *i.e.* meshes can either be structured or unstructured. Equation 15, can reciprocally be written for $i \in \Omega_{\widetilde{\mathcal{V}}}$.

Even though this formulation results from a conservative assumption, the resulting procedure is not fully conservative as it has been demonstrated that the only conservative Chimera approach is based on flux interpolation [30, 31, 56], rather than conservative variable interpolation as employed here. Nonetheless, using an integral formulation for transferring solution is consistent with the finite volume approach.

3.2.5. Modified K-Dubois limiter for Chimera interpolation

As mentioned previously, reconstructions, on the one hand, of the solution for solving the Riemann problem at cell interfaces 9 and, on the other hand, of the ghost cell solution through the 2nd order Chimera method 15 require a limiting procedure to satisfy TVD constraint and avoid occurence of local extrema. To avoid a possible limitation on mesh constructions and to make the method suitable for both structured and unstructured meshes, we have privileged *the K-Dubois* limiter [51] that acts on the primitive variables. Let us underline that a more commonly used limiter, namely the Jespersen & Barth limiter [57], would also be suitable for the present method.

In the standard finite-volume implementation of the K-Dubois limiter [51], values $\mathbf{w}_i^{\min} = \min(\mathbf{w}_i, (\mathbf{w}_j)_{j \in \gamma(i)})$ and $\mathbf{w}_i^{\max} = \max(\mathbf{w}_i, (\mathbf{w}_j)_{j \in \gamma(i)})$ need to be computed. Then the solution $\mathbf{w}_i$ should obviously verify:

$$\mathbf{w}_i^{\min} \leq \mathbf{w}(x, y, z)_i \leq \mathbf{w}_i^{\max}. \tag{16}$$

The K-Dubois limiter [51] is expressed as:

$$\Phi_i = \min\left(1, K \cdot \frac{\min(\mathbf{w}_i^{\max} - \mathbf{w}_i, \mathbf{w}_i - \mathbf{w}_i^{\min})}{\max_{j \in \gamma(i)}(\nabla \mathbf{w}_i \cdot (\mathbf{x}_{(face)_{ij}} - \mathbf{x}_i))}\right). \tag{17}$$

As indicated by [51], the parameter K allows the limiter to be more flexible than the Barth and Jespersen limiter [57] as it can modify the behavior of the limiter to make it more or less compressive [1]. In this paper, we set the parameter K to 0.75 as recommended in [51] and used in [58, 59]. The quantity $(\mathbf{x}_{(face)_{ij}} - \mathbf{x}_i)$ represents the distance between the center of the cell face s_{ij} and the cell center $\mathbf{x}_i$. Taking the maximum value of $(\mathbf{x}_{(face)_{ij}} - \mathbf{x}_i)$ among all faces of the considered cell ensures that the solution is limited in the sense of equation 16. This implies that

[1] By more compressive, we mean that the limiter is capable to capture more accurately a contact discontinuity or a shock by reducing the numerical diffusion of the numerical scheme.

the limited reconstructed solution can be searched inside a neighborhood (*i.e.*... a circle in 2D, and a sphere in 3D) with a typical radius of $R = \max_{j\in\gamma(i)}(\mathbf{x}_{(face)_{ij}} - \mathbf{x}_i)$ (see figure 6).

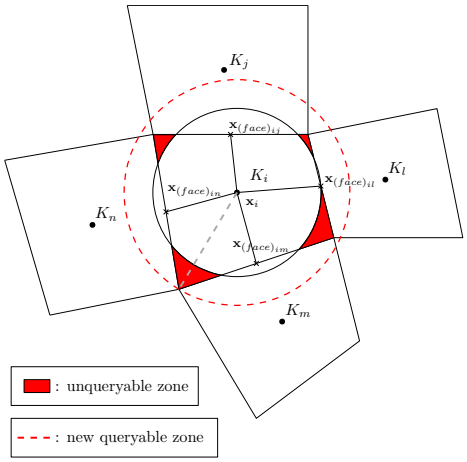

Figure 5: Search area for the K-Dubois limiter in a single model approach. The searchable area is identical for the Barth and Jespersen limiter [57].

Nevertheless when several overlapping grids are at play, the previous constraint applied to the solution is not restrictive enough to enforce non-oscillatory property, and the search zone must be enlarged to recover TVD property as it is shown in figure 6. In fact, when refining the patch $\mathcal{V} = \{K_k^{'}\}_{k\in\Omega_{\mathcal{V}}}$, ghost cells can be intersected by a cell portion that can be outside of the search region, K_i in this example. The reconstruction then gives:

$$\widetilde{\mathbf{v}}_k^n = \frac{|\widetilde{K}_k \cap K_i^{'}|}{|\widetilde{K}_k|}\Big(\mathbf{w}_i^n + \Phi_i\nabla(\mathbf{w}_i^n)(\widetilde{\mathbf{x}}_{ki} - \mathbf{x}_i)\Big) + \sum_{p\in\Omega_{\mathcal{W}}\setminus\{i\}} \frac{|\widetilde{K}_k \cap K_p^{'}|}{|\widetilde{K}_k|}\Big(\mathbf{w}_p^n + \Phi_p\nabla(\mathbf{w}_p^n)(\widetilde{\mathbf{x}}_{kp} - \mathbf{x}_p)\Big). \quad (18)$$

Here, we can see that $|\widetilde{\mathbf{x}}_{ik} - \mathbf{x}_i|$ can be greater than $|\mathbf{x}_{(face)_{ij}} - \mathbf{x}_i)\big|$ depending on the location of cells. This is also emphasized by increasing χ. In those particular cases, the limiter is not adapted as the solution will be searched outside the search zone described in figure 5. Thus, the transfer can generate local extrema.

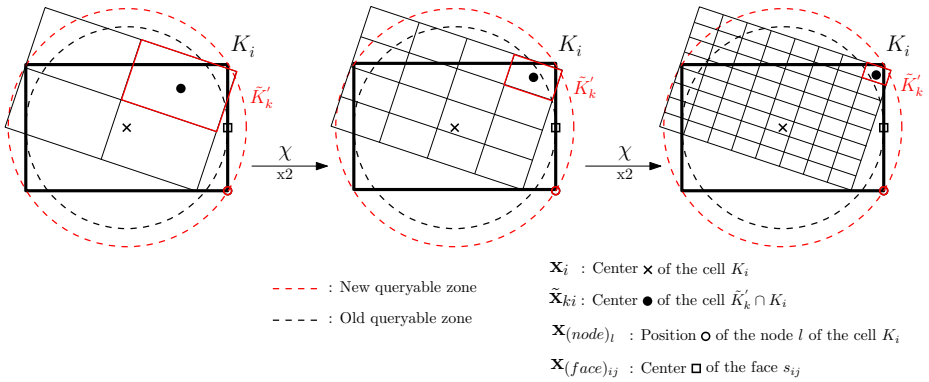

Figure 6: Evolution of the positions between the center of the intersection with the sending cell and the center of the sending cell.

We propose to recast the previous limiter 17 to make it work with the present Chimera method. The limiter is then recast as follows:

$$\Phi_i = \min\left(1, K \cdot \frac{\min(\mathbf{w}_i^{\max} - \mathbf{w}_i, \mathbf{w}_i - \mathbf{w}_i^{\min})}{\max_{l\in\eta(i)}(\nabla\mathbf{w}_i \cdot (\mathbf{x}_{(\text{node})_l} - \mathbf{x}_i))}\right). \tag{19}$$

The new version of the K-Dubois limiter adapted to the present Chimera method is based on the radius calculated from the cell corners instead of centers of cell faces. The radius of the search region is now enlarged with an extended radius $R = \max_{l\in\eta(i)}(\mathbf{x}_{(\text{node})_l} - \mathbf{x}_i)$, where $\mathbf{x}_{(\text{nnode})_l}$ is the cell corner coordinates, and $\eta(i)$ is the corner set of the cell K_i (see figure 5). This extents the search zone of the limited solution so as to be valid whatever the location of the ghost cell and the cell ratio are.

4. Numerical results

To assess the present approach, we select five well-known test cases from the literature. Each test case is chosen to stress the method on one particular aspect in order to highlight capabilities and limitations of the present Chimera method. Every case involves flow structures crossing the Chimera interface. A 1D advection of a density profile is first used to check the order of accuracy of both the numerical scheme and the proposed Chimera method. A stationary shock coinciding with the patch interface helps assessing conservation properties. The supersonic flow around a 2D cylinder is then undertaken with an overlapping grid in the vicinity of the cylinder. The fourth test case concerns the interaction of a shock wave in Air with a bubble initially cylindrical and filled with Helium. This allows us to stress the good behavior of the present method to deal with fast transient dynamics of multi-component flows. At last, the well known test case of the double Mach reflexion is undertaken with overlapping grids. We can thus check the ability of the method to account for multiple interactions between discontinuities even if they move across the overlap grid boundaries.

4.1. 1D - Sinus Advection

In order to assess the order of accuracy of the numerical scheme, and the impact of the interpolation used in the Chimera exchange on the global order of convergence, the linear advection of a smooth analytical solution is considered similarly as in [60, 58, 59]. We superimpose a regular fluctuation on the density field that is convected with a constant velocity:

$$\begin{array}{rcccl} \rho & = & \rho_0(1+\delta_\rho) & & \\ u & = & u_0 & = & 100 \text{ m.s}^{-1} \\ p & = & p_0 & = & 1 \text{ bar} \end{array} \tag{20}$$

with the normalized density fluctuation given by,

$$\delta_\rho = \begin{cases} A \sin^2(\frac{\pi x}{l}) & \text{if } 0 \leq x \leq l \\ 0 & \text{elsewhere,} \end{cases} \tag{21}$$

where $A = 10^{-2}$ is the amplitude of the perturbation, $l = L/5$ the length on which the density is perturbed, T is the period of the perturbation and $L = u_0 T = 10$ m is the length of the computational domain $[0, L]$. For the present exemple, the initial center of the perturbed density region is located in $x_c = 0.1L$, as seen in figure 7. The simulation stops at $t_f = 0.7T$ which is the time for which the center of the density fluctuation is located at $x_c = 0.8L$.

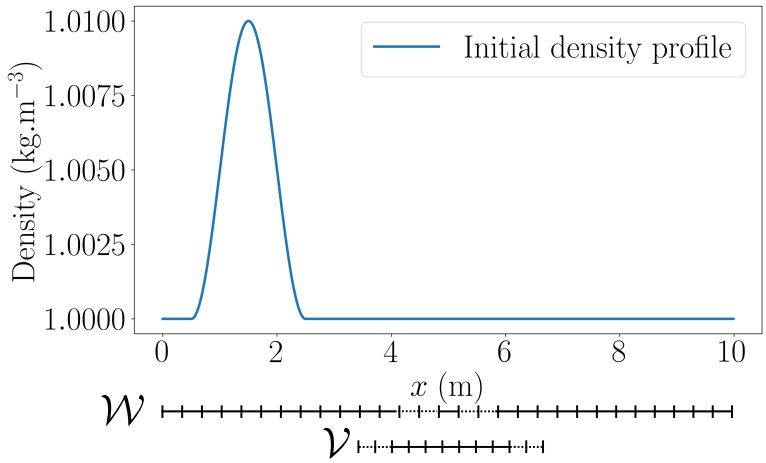

Figure 7: Sinus advection test case: initial solution and grid arrangements for the chimera configuration.

Computations have been performed on both a single grid domain (without any patch), and with a patch that is located centered on the substrate, from $x_1 = 1/3L$ to $x_2 = 2/3L$ as it is shown in figure 7. On the substrate, we used 6 different grids from the coarsest $Ncells = 100$ cells regularly distributed on L to the finest using $Ncells = 3200$ cells, *i.e.* the grid spacing evolves with power of 2 between two meshes. We note $Ncells$ the number of grid cells along the substrate. As we would like to highlight the spatial accuracy, whatever the grid is, a constant time step $\Delta t = 10^{-5}$ s has been used for lowering the time integration error.

First, we set the cell ratio between the patch and the substrate to $\chi = 1$, and we consider that the mesh on the patch is not coincident with the mesh on the substrate (see Fig. 7 for a sketch). This allows us to study the grid convergence as well as the impact of the Chimera interpolation on the global accuracy.

At the final time t_f, we compare numerical solutions obtained on both the single grid configuration (only the substrate is considered) and the configuration with the patch superimposed on the substrate, to the analytical solution which is the simple convection of the initial density profile without any diffusion. To measure numerical errors, we calculate the L_1 norm of the density error, computed as follows:

$$L_1(\varepsilon_\rho) = \int_0^L |\rho_{\text{num}} - \rho_{\text{th}}|\, dx \approx \sum_{i=0}^{\Omega_W} |\rho_i - \rho_{\text{th}}(x_i)|\Delta x, \tag{22}$$

where ρ_{th} is the analytical density profile and ρ_{num} the numerical density solution. The evolution of the L_1 norm of density errors versus the grid spacing is plotted in figure 8. On the one hand, for the single mesh configuration (without any patch), the second-order of accuracy is clearly recovered for finest grids (at least from 800 grid points over L) by using the 2nd-order Godunov approach based on a MUSCL scheme. On the other hand, using the present Chimera method on a patched configuration on 1/3 length of the computational domain does not seem to notably deteriorate the order of accuracy of the original method. As the interpolation of ghost cell solutions between two facing grids is 2nd-order accurate, the global order of accuracy is almost recovered although slight discrepancies compared to single grid results can hardly be noticed in the coarsest grid configurations (Fig. 8). To judge the very low intensity of these discrepancies, we report in

table 1 the L_1 density errors as well as the measured order of accuracy. As mentioned earlier, the

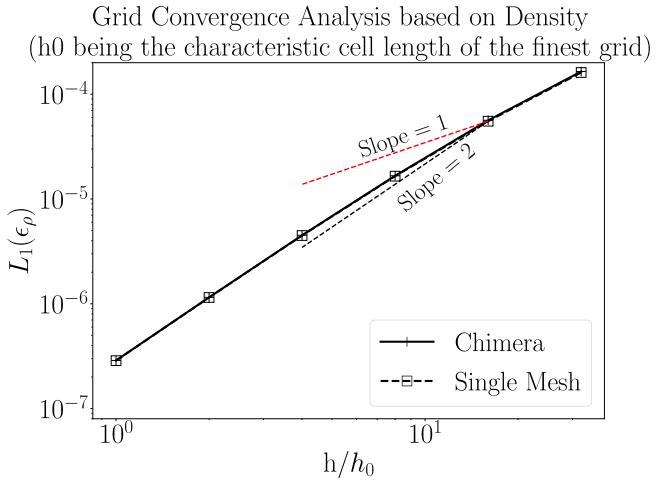

Figure 8: Grid convergence analysis of the sinus advection case for the first study ($\chi = 1$).

second-order of accuracy is achieved with at least 800 grid points even if a Chimera method is employed with a non-coincident patched grid.

Table 1: Grid convergence analysis: results on density (ρ) errors obtained with a single grid configuration as well as with the present Chimera approach using a patch with same grid spacing as the substrate ($\chi = 1.0$) but with non-coincident grids.

Ncells	L_1 error		Order of convergence p	
	Single	Chimera	Single	Chimera
100	1.609e-4	1.643e-4	1.595	1.551
200	5.499e-5	5.607e-5	1.755	1.770
400	1.629e-5	1.644e-5	1.909	1.913
800	4.338e-6	4.366e-6	2.022	2.026
1600	1.068e-6	1.072e-6	2.119	2.108
3200	2.459e-7	2.487e-7	-	-

Secondly, we prescribe the cell number on the substrate to $Ncells = 200$, and refine the grid on the patch in order to assess the impact of the transfer between a coarse substrate and a finer patch which seems to be the most sought-after configuration. Cell ratios between the patch and the substrate spread from $\chi = 1$ which is the previous situation where grid spacing is identical on the patch and on the substrate with however non-coincident grids, to $\chi = 16$ where the grid spacing on the patch is 16 times smaller than on the substrate. Results on the L_1 norm of density errors are reported in Table 2. The last column reports the equivalent number of cells ($Ncells$) that would be needed on the substrate to recover the same grid refinement as used in the patched region. Let us recall that solution errors are calculated at $t_f = 0.7T$ once the density profile passed through the patch and completely left the patch, situated from $x_1 = 1/3L$ to $x_2 = 2/3L$. That way, errors obtained must mainly be compared to the ones of single grid configuration with $Ncells = 200$ cells. Refining the patch slightly increases the accuracy of the overall results while it is obvious that solution errors are mostly dominated by the ones generated on the coarser grid

Table 2: L_1 norms of density error obtained with the present Chimera approach using a patch with several cell ratios between the patch and the substrate ($1 \leq \chi \leq 16$); the substrate comprises $Ncells = 200$ gris cells.

Ratio χ	$L_1(\varepsilon_\rho)$ error	Equivalent $Ncells$ on the patch
1	5.607e-5	200
2	4.405e-5	400
4	4.135e-5	800
8	4.032e-5	1600
16	4.014e-5	3200

of the substrate. In other words, this however emphasizes that errors due to Chimera exchange between the two facing grids do not impact the global solution error when the patch is finer than the substrate.

4.2. Conservation properties of the present Chimera method

Although our local conservation hypothesis is not sufficient to ensure global conservation of the system [30, 31, 56], we verify in this section that the Chimera method does not introduce conservation error with coincident grid interfaces. Then, we verify that the conservation error due to the Chimera exchange with non-coincident grid interfaces and variable cell ratios meet acceptable levels for industrial requirements.

To this end, we study the behavior of the finite volume Chimera formulation when a steady shock wave is located at the patch interface. This 1D test case is taken from [61] and [42]. The full computational domain is $-5 \leq x \leq 5$ and it is discretized in two regions of $Ncells = 25$ each for the single grid configuration.We note $h_{\mathcal{W}}$ and $h_{\mathcal{V}}$ respectively the cell size of $\mathcal{W}$ and $\mathcal{V}$. We define the exchange zone shift δ_S as:

$$\delta_S = \delta_{GC} - \frac{1}{2}(h_{\mathcal{W}} + h_{\mathcal{V}}). \tag{23}$$

The interface between the two regions is located at $x = 0$ and the chimera configurations are depicted in figure 9 with coincident grid interfaces ($\delta_S = 0$) and non-coincident grid interfaces ($\delta_S \neq 0$) with $\chi = 2$. For every Chimera grid configuration, the patch interface is fixed and coincide with the shock wave discontinuity at $x = 0$. The variable $Ncells$ also corresponds to the number of cells on the substrate while the number of cells on the patch is defined by the cell ratio χ. The flow states on each side of the discontinuity are the following:

$$\begin{cases} (\rho, u, p)_L &= (1\,\text{kg.m}^{-3}, 1.5\,\text{m.s}^{-1}, 0.71429\,\text{Pa}), \\ (\rho, u, p)_R &= (1.8621\,\text{kg.m}^{-3}, 0.8055\,\text{m.s}^{-1}, 1.7559\,\text{Pa}). \end{cases} \tag{24}$$

As the shock discontinuity coincides with the patch interface, the patch contains exclusively the right state of the shock. All simulations are performed up to a dimensionless time $t^\star = t\,u_L/L = 100$, using a prescribed CFL number CFL $= 0.4$ on both the single grid configuration and the overlapping grids. This time ensures a converged solution with residuals of density, momentum and total energy lower than 10^{-9} on every case. The error on conservation is

computed for each conservative variables as the following:

$$\begin{aligned}
\varepsilon(\rho(t^\star)) &= \frac{\left|\int \rho(t^\star,\mathbf{x})\,dV - \int \rho(0,\mathbf{x})\,dV\right|}{\int \rho(0,\mathbf{x})\,dV} \\
\varepsilon((\rho u)(t^\star)) &= \frac{\left|\int (\rho u)(t^\star,\mathbf{x})\,dV - \int (\rho u)(0,\mathbf{x})\,dV\right|}{\int (\rho u)(0,\mathbf{x})\,dV} \\
\varepsilon(\rho E(t^\star)) &= \frac{\left|\int (\rho E)(t^\star,\mathbf{x})\,dV - \int (\rho E)(0,\mathbf{x})\,dV\right|}{\int (\rho E)(0,\mathbf{x})\,dV}
\end{aligned} \tag{25}$$

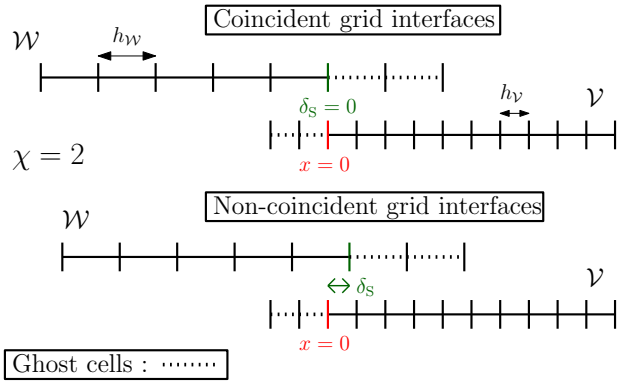

Figure 9: Stationary shock grid configuration for coincident grids and non-coincident grids with the shock located at $x = 0$.

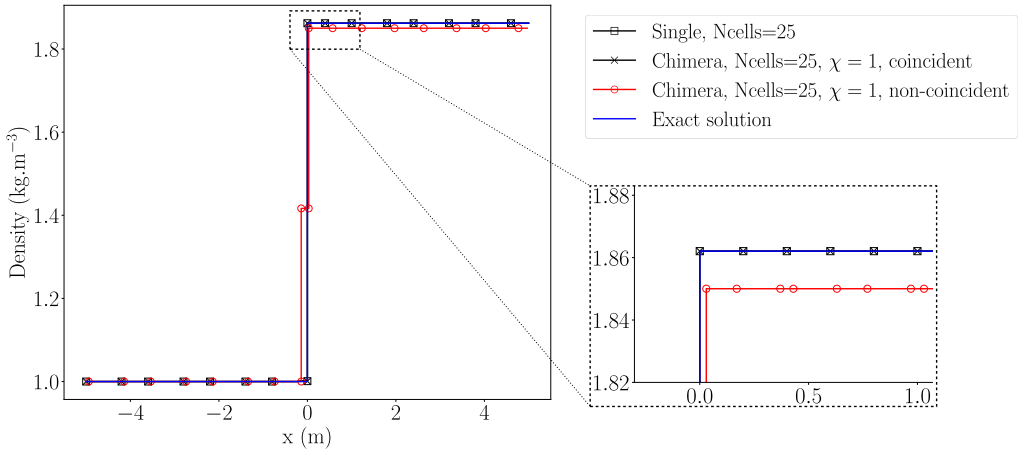

Figure 10: Density profile of the stationary shock converged solution in a single grid configuration with $Ncells = 25$ and a Chimera configuration with coincident and non-coincident grids for $Ncells = 25$ and $\chi = 1$ compared to the exact solution.

In figure 10, we show the results of the Chimera configurations with coincident grid interfaces and non-coincident grid interfaces with equivalent cell size compared to the single mesh configuration ($Ncells = 25, \chi = 1$) and the exact solution. As highlighted by the table 3, conservativity

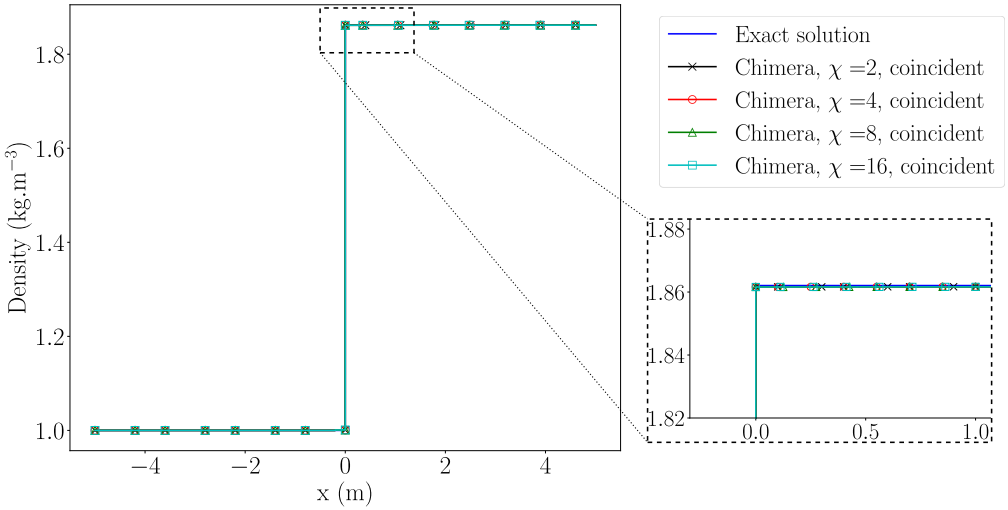

(a) Coincident grid interfaces

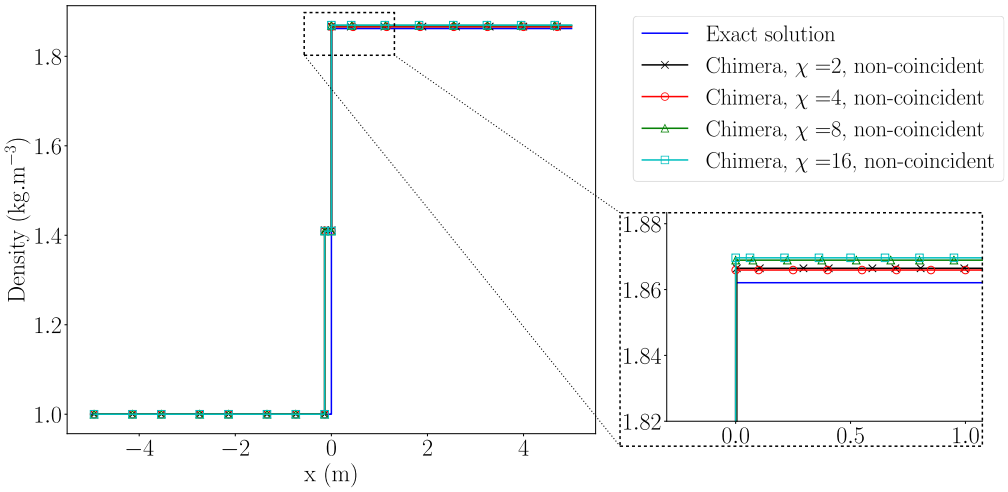

(b) Non-coincident grid interfaces

Figure 11: Density profile of the stationary shock converged solution in a Chimera configuration with coincident and non-coincident grids for $Ncells = 25$ and χ varying from 2 to 16 compared to the exact solution.

is preserved on mass, momentum and total energy for the coincident grid interface case as seen in figure 10 with identical errors compared to the single mesh case. It is obvious that the Chimera method with non-coincident grid interfaces introduces conservation error since a maximum of about 0.6% is recorded on the conservation error of momentum. In fact, the shockwave is still located at the patch interface but at the same time, is also located within a coarse cell of the substrate that induces higher error levels. When refining the patch ($\chi = 2, 4, 8$ and 16) with coincident grids, we can observe from table 4, that total mass, momentum and energy are relatively preserved with an error of the same order of magnitude as the single grid configuration which is

10^{-4}%. As the shock diffuses upstream in the substrate grid when non-coincident grid interfaces are used, refining the patch has only a weak effect on error levels. The error magnitude is however relatively low since it does not exceed 1%. To put those results in perspective, figure 11 (b) shows the impact of the Chimera method on the post-shock state with non-matching grids. The loss on the density jump is at most 0.35% of the exact post-shock state which is acceptable for industrial applications.

Table 3: Total mass, momentum and energy error computed on the converged solution with a single grid configuration as well as with the present Chimera approach using a patch with the same grid spacing as the substrate ($Ncells = 25$, $\chi = 1.0$) with a shock matching the patch boundary.

	$\varepsilon(\rho(t^\star))$ in %	$\varepsilon((\rho u)(t^\star))$ in %	$\varepsilon((\rho E)(t^\star))$ in %
Single	5.9708302e-4	2.4492026e-3	4.4632114e-3
Chimera (coincident grids)	5.9708302e-4	2.4492026e-3	4.4632114e-3
Chimera (non-coincident grids)	4.3402693e-1	6.3486174e-1	4.6451928e-1

Table 4: Total mass, momentum and energy error computed on the converged solution with a single grid configuration as well as with the present Chimera approach using a patch with different grid spacings and a shock matching the patch boundary.

χ	Chimera (coincident interfaces)			Chimera (non-coincident interfaces)		
	$\varepsilon(\rho(t^\star))$ in %	$\varepsilon((\rho u)(t^\star))$ in %	$\varepsilon((\rho E)(t^\star))$ in %	$\varepsilon(\rho(t^\star))$ in %	$\varepsilon((\rho u)(t^\star))$ in %	$\varepsilon((\rho E)(t^\star))$ in %
1	5.970e-4	2.449e-3	4.463e-3	4.340e-1	6.349e-1	4.645e-1
2	6.110e-4	3.113e-3	3.344e-3	1.331e-1	3.223e-1	3.185e-1
4	6.154e-4	3.175e-3	3.815e-3	1.152e-1	3.899e-1	4.271e-1
8	6.176e-4	3.209e-3	4.062e-3	2.183e-1	5.589e-1	5.628e-1
16	6.189e-4	3.225e-3	4.189e-3	2.422e-1	5.987e-1	5.949e-1

4.3. Flow around a circular cylinder at Mach = 3

A circular cylinder with a radius $D = 1$ m, is initially placed in Air ($\gamma = 1.4$) which is assumed as a perfect gas. A shock wave is initially located 8 cylinder diameters in front of the cylinder with a flow at Mach $M_\infty = 3$ upstream of the shock wave. Infinite pressure and density are prescribed, respectively at $P_\infty = 96774$ Pa, and $\rho_\infty = 0.519\,\mathrm{kg.m^{-3}}$ upstream of the shock wave. Initial conditions downstream this shock wave, around the cylinder, are prescribed by using the Rankine-Hugoniot relationships assuming that the front shock wave moves towards the cylinder with a Mach number equal to $M_{\mathrm{sh}} = 1$. The initial state of this test case is shown in figure 12 where we see the computational domaine $(x \times y) \in [-10, 10]^2$ m $\times$ m.

A grid that fits both the body and external domain boundaries is first built to serve as a single-grid configuration. A zoom-in view in the vicinity of the cylinder is provided in figure 13-(a), where we see the transition between a O-grid very close to the cylinder towards a H-grid far away. In the followings, we use the number of grid cells ($Ncells$) distributed along the cylinder perimeter as the parameter to refer as refinement. We then built the grid of the patch, attached to the cylinder with a O-grid that at most coincides with the single-grid configuration very close to the cylinder to facilitate comparisons with the single grid model (see in Fig. 13-(a) the grid in red superimposed to the single grid configuration). Then the substrate model employed in the Chimera computation is a Cartesian grid that fits the external boundaries of the computational domain, as we can see in figure 13-(b), where a zoom-in close to the cylinder is presented showing the patch grid superimposed to the substrate model. Let us remark that, when considering

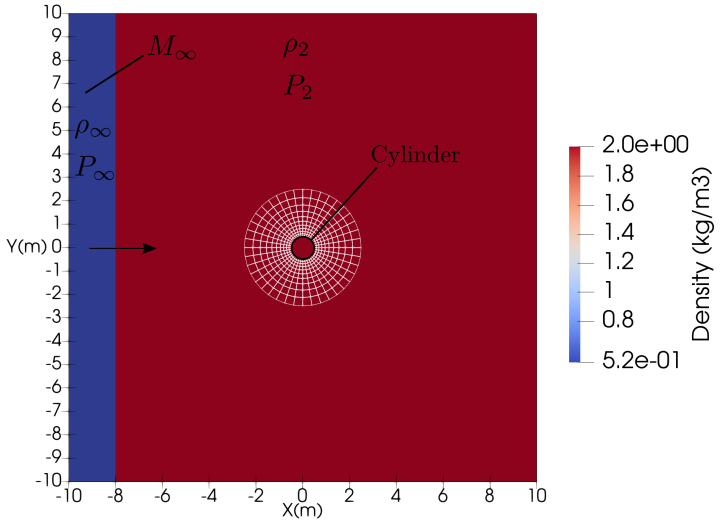

Figure 12: The circular cylinder test case: computational domain and the initial solution.

the problem with overlapping domains, the cylinder only belongs to the patch domain and does not explicitly appears in the substrate model.

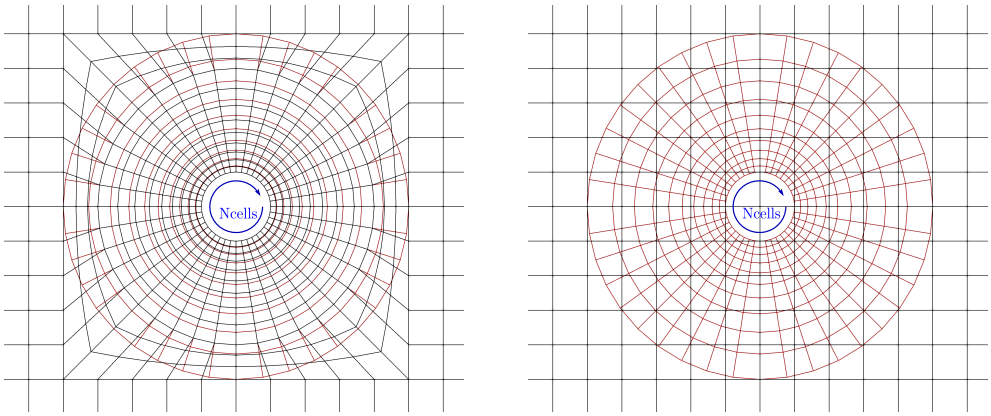

(a) Single mesh case vs Patch **(b)** Chimera case

Figure 13: Grid configuration for the single mesh case and the Chimera case.

All simulations are performed up to a dimensionless time $t^\star = t\,u_\infty/L = 52.5$ (where u_∞ is the infinite velocity), using a prescribed CFL number CFL $= 0.4$ on both the single grid configuration and the overlapping grids.

At first, we keep the cell ratio between the patch and the substrate close to unity, meaning that the minimum grid spacing used in the patch (along the cylinder perimeter) is the same as the one used in the substrate although meshes are not coincident away from the cylinder, as we can see in figure 13-(b). Several grid resolutions are employed from $Ncells = 50$ along the cylinder

perimeter to $Ncells = 400$, to study grid convergence.

Steady state solutions are presented in figure 14, on the density contours obtained at a dimensionless time $t^\star = 52$ and for $Ncells = 200$ grid cells along the cylinder perimeter between, with the single-grid configuration (on the left), and the overlapping grids (on the right). As we can see, results seem to be similar, and it is hard to differentiate them following the density contours. Let us first remark that in the Chimera case, when the front shock wave passes through the interface from the substrate to the patch, no spurious reflection is generated, meaning that the present Chimera method is able of dealing with wave propagation across grid interfaces.

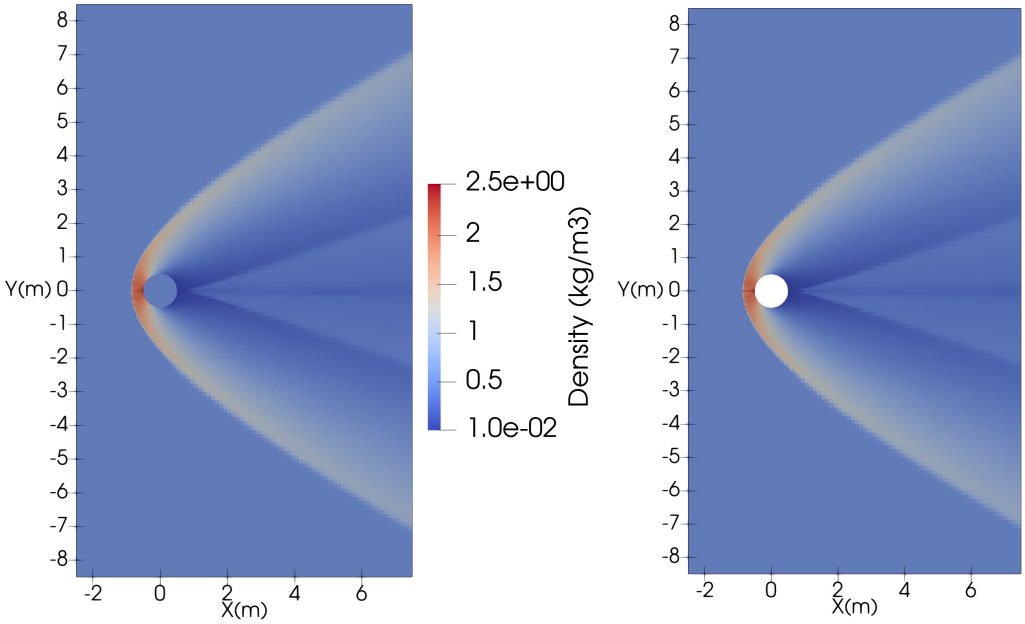

(a) Chimera case **(b)** Single mesh case

Figure 14: Steady state density field for both single grid case (on the left), and the overlapping grids (on the right) with a cell ratio of unity ($\chi = 1$), obtained at a dimensionless time $t^\star = 52$ and for $Ncells = 200$ grid cells along the cylinder perimeter.

To get a better validation of results obtained with the Chimera method, we use an integral quantity based on the pressure drag force exerted by the flow on the cylinder, calculated at each time step. Time history of this pressure drag force is plotted in figure 15.

When the moving front shock wave interacts with the cylinder, a peak on the pressure drag force occurs, followed by a relaxation period during which the front shock wave comes established as a bow shock in front of the cylinder. Then a steady state solution occurs. Whatever the grid spacing is, a statistically converged steady state solution is achieved from at most a dimensionless time $t^\star = 35$, with however the finer the grid, the greater this time occurs. As we can see, for the coarsest grids the drag force converges towards a constant value while for the finer grids oscillations around a converged value appear due to the high resolution of the cylinder wake. Compared to the single grid computations, the Chimera method gives comparables results on the drag force while some weak discrepancies can be recorded for the coarsest grids. Very

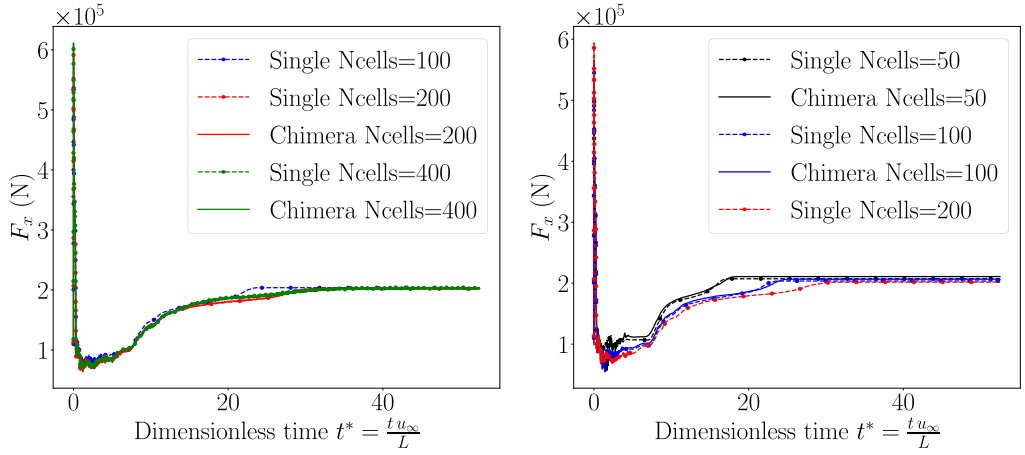

Figure 15: Time history of the pressure drag force for several number of grid cells (*Ncells*) obtained on both the single-grid configuration, and the ovelapping grids with however similar grid spacings ($\chi = 1$).

similar results have however been recovered for the finest grid tested with the Chimera method. By zooming in on the steady state region between dimensionless times 40 and 52.5 as shown in figure 16, we can see that the average force seems to converge toward the value $F \approx 202 \times 10^3$ N. We can observe that the Chimera case captures oscillations around the cylinder with a coarser grid refinement than the single grid configuration. Considering that grids between the single mesh case and the Chimera case are similar but not identical, differences might be caused by a difference in the grid resolution as well as a better grid regularity of the mesh in the Chimera case.

On table 5, we have reported the averaged force calculated for several number of cells over the cylinder perimeter (*Ncells*), over the time interval $t^\star \in [40; 52.5]$ for both the single mesh case and the Chimera case. Relative differences, w.r.t. the single grid case, between the overlapping case and the single grid configuration are reported in the last column as percentages. Discrepancies between the single mesh case and the Chimera case decrease as grids are refined. For grids for which solutions are considered as converged ($Ncells \geq 200$), discrepancies are very small which fulfill our expectations, especially since meshes employed in Chimera method are less distorted, possibly creating less approximation errors.

Table 5: Average resulting pressure force over $t^\star \in [40; 52.5]$ for the first study cases ($\chi = 1$).

Ncells	$\frac{1}{t_2-t_1}\int_{t_1}^{t_2} F(t)\,dt$ (N)		% difference with Single
	Single	Overlap	
50	207328	210871	1.7 %
100	203606	206604	1.47 %
200	201774	202320	0.27 %
400	203000	202164	0.47 %

Secondly, we set $Ncells = 100$ on the substrate model and vary χ values of the overlapping grid, $\chi = 1, 2$, and 4, which corresponds to refine the patch with equivalent number of cells along the cylinder perimeter, respectively $Ncells = 100, 200$, and 400. In other words, it corresponds

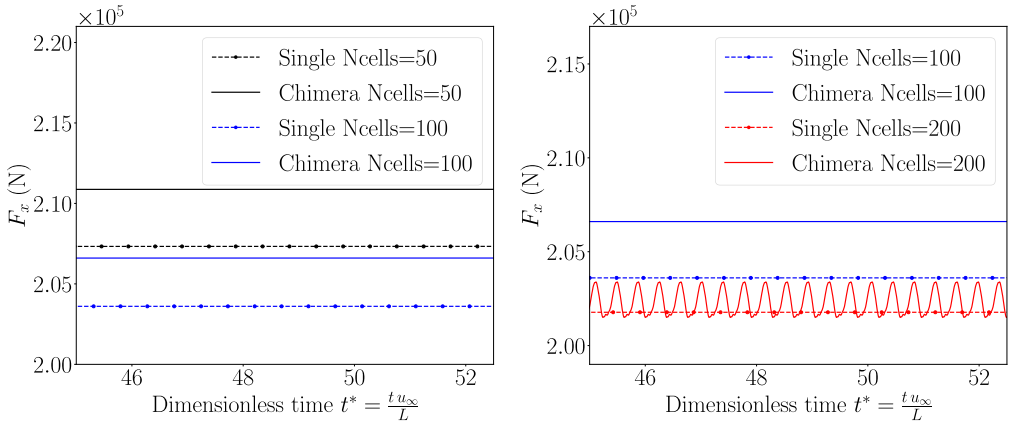

(a) *Ncells* = {50, 100}

(b) *Ncells* = {100, 200}

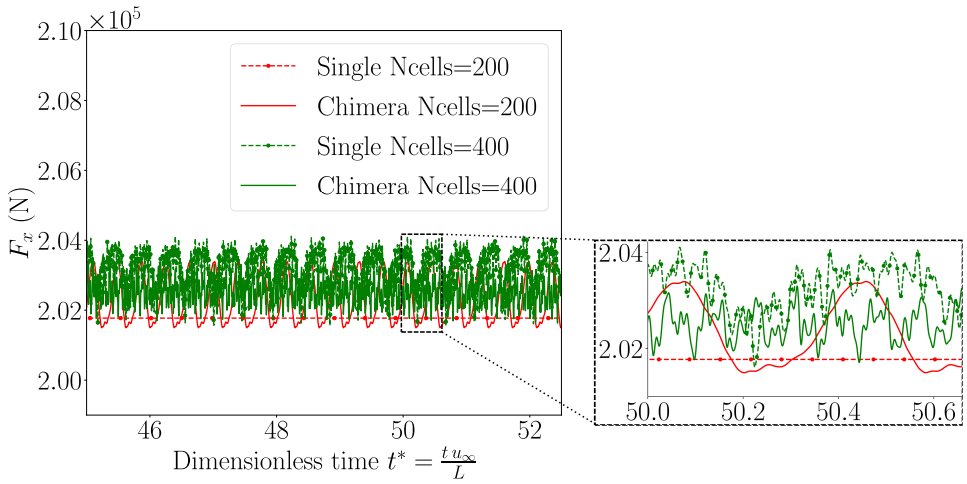

(c) *Ncells* = {200, 400}

Figure 16: Zoom in the interval dimensionless times $t^\star \in [45\,;52.5]$ of the pressure drag force history for several number of grid cells (*Ncells*), obtained on both the single-grid configuration, and the ovelapping grids with however similar grid spacings ($\chi = 1$).

to a patch refinement over a constant grid spacing substrate. In figure 17, we plot histories of the drag force on the cylinder obtained on several refined overlapping grids compared with the equivalent fine single mesh (EFSM) with the same number of cells along the cylinder perimeter. Refining the patch does not introduce local perturbation but instead increases the accuracy of the resulting force as the regularity of the mesh is better ensured than in a single case for the same *Ncells* (see Fig. 13).

To better examine predicted converged values of the drag force, we plot a zoom in of histories in between $t^\star \in [45\,;52.5]$ obtained with both the overlapping grids with cell several ratios and the equivalent fine single mesh (Fig. 18). Similar results as with the Chimera case with $\chi = 1$ are

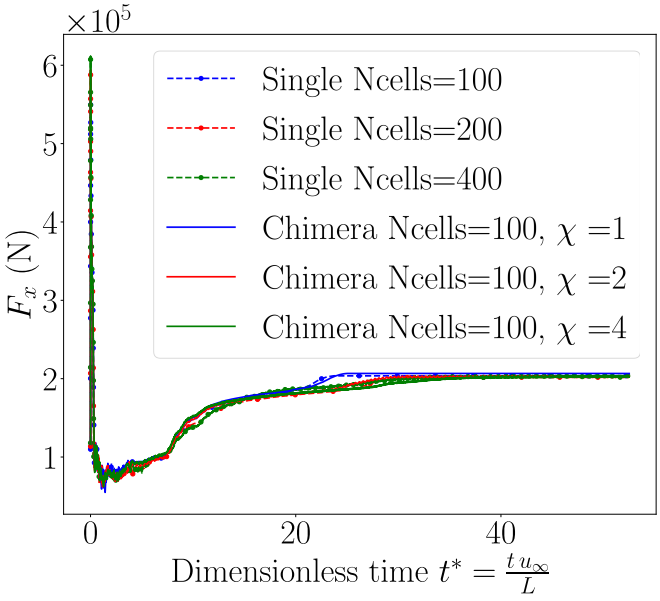

Figure 17: Resulting pressure force over time for the second study cases (*Ncells* = 100).

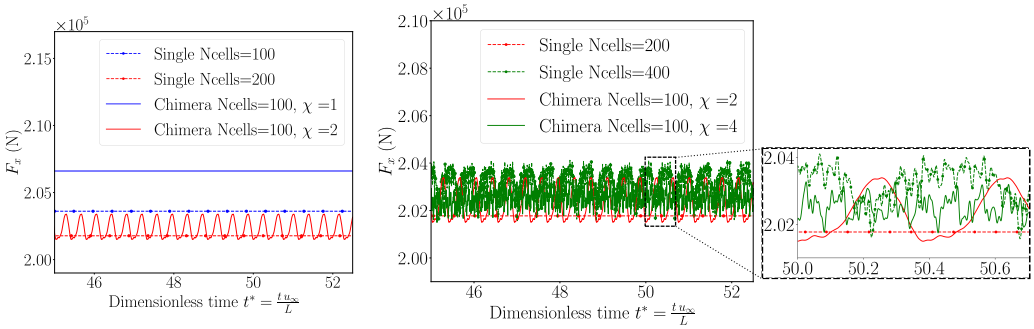

Figure 18: Resulting pressure force over time for the second study cases ($\chi = 1$) zoomed in the time interval [45 ; 52.5].

obtained that compare very well with the equivalent fine single grid cases. In fact, as reported in table 6, comparable discrepancies with respect to the equivalent single grid computations are recorded by the refined Chimera case ($\chi \neq 1$) compared to the results obtained with $\chi = 1$. Nevertheless, the force of the Chimera method allows to predict results with the similar accuracy at however a much less computational cost since less grid points are necessary for the same grid spacing. This is confirmed in table 6, where we report the ratios of the CPU times for the equivalent fine single grid to the CPU time of the corresponding Chimera configuration when χ varies. The ratios of the memory usage for the equivalent fine single grid to the memory usage of the corresponding Chimera configuration when χ varies are also reported. When $\chi =$ 1, the ratio is less than 1 expressing that the Chimera method costs more than the single grid

Table 6: Results obtained with the Chimera cases ($Ncells = 100$), compared with their equivalent fine single grid computations.

χ	Chimera Average F	$Ncells$ EFSM	Error (%) compared to EFSM	CPU time ratio	CPU memory ratio
1	206604	100	1.47 %	0.97	0.97
2	202314	200	0.27 %	2.3	2.41
4	201966	400	0.5 %	3.5	3.8

computation because of a higher number of grid cells, interpolation and transfer of ghost cell solutions. However, compared to single mesh computations with same grid resolutions, once we increase χ, equivalent results are obtained at a much lower cost, mainly coming from the gain in the number of grid points since the time step is equivalent because the grid spacing is the same. Even though the present Chimera method is not intended to grid optimization, the method allows significant gains in time and memory without impacting the resulting solution.

To have a better local insight in present results, we measure the detachment distance of the bow shock wave in front of the cylinder. A sketch of the flow structure in front of the cylinder is proposed in figure 19, where the detachment distance (δ) of the bow shock wave is defined. An analytical measurement of the shock wave standoff distance has been proposed by Sinclair and Cui [62], that provides with $\delta = 0.3649D$ at an infinite Mach number $M_\infty = 3$.

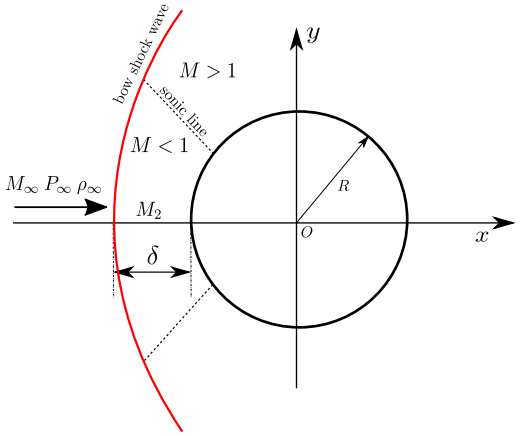

Figure 19: Geometric illustration of the flow structure in front of the cylinder.

From our results, we measured the detachment distance along the horizontal axis of symmetry ($y = 0$) as the first point encountered from infinity where the pressure rise exceeds 50 % of the theoretical pressure jump across the shock wave. Detachment values (δ) recorded on Chimera results are reported in Table 7. The left side of the table refers to overlapping grids with similar cell ratio ($\chi = 1$) while the right side relates on results obtained by increasing the cell ratio (χ) with $Ncells = 100$ grid cells along the cylinder perimeter in the substrate model. Numerical values of δ converge towards the analytical value [62] as grids are progressively refined with a discrepancy close to 2 % of the analytical value obtained for the finest grid. Using O-grid is certainly not the best mesh to accurately capture the bow shock wave that may explains why relative errors don't seem so small. A more suitable grid for the patch could probably have been

Table 7: Detachment distance of the bow shock wave in front of the cylinder: overlapping grids with the proposed Chimera cases. On the left side, number of cells are increased keeping the cell ratio ($\chi = 1$) constant. On the right side, cell ratio (χ) is varied with a prescribed number of cells in the substrate model ($Ncells = 100$).

Overlapping grids with $\chi = 1$, and $Ncells$ is varied:		
Ncells	δ/D	relative error E (%) w.r.t. analytical value
50	0.433	18.66
100	0.428	17.29
200	0.398	9.07
400	0.372	1.95

$Ncells = 100$ in the substrate model and χ is varied:		
χ	δ/D	relative error E (%) w.r.t. analytical value
1	0.428	17.29
2	0.395	8.25
4	0.372	1.95

used, but this is not the purpose of this work. What is important to underline is that, compared to overlapping grids with equivalent cell ratio ($\chi = 1$), same δ values have been recorded by using a refined patch model keeping a rather coarse substrate grid at a much smaller computational cost which is promising for target applications.

4.4. Interaction of a shock wave moving in Air with a Helium bubble,

In order to assess the Chimera method with two-phase flow interfaces, we have numerically reproduced one of the emblematic experiments originally proposed by Haas and Sturtevant [63] and more recently conducted by *Layes et al.* [64], where a shock wave moving at a Mach number $M_a = 1.22$ in Air interacts with a cylindrical bubble initially filled of Helium. The initial configuration is depicted in figure 20. The computational domain is defined as $(x \times y) \in$

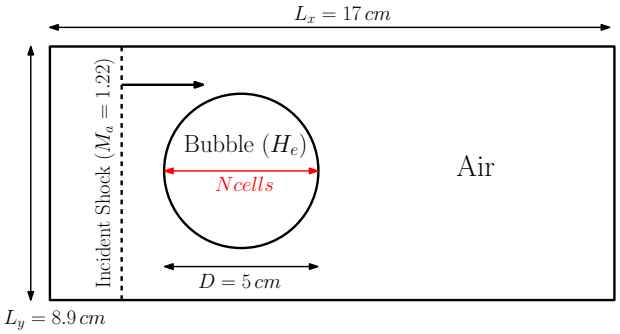

Figure 20: Shock wave / Bubble interaction: initial conditions taken from Layes *et al.* experiments [64] and computational domain.

$[-44.5 \times 10^{-3}; 44.5 \times 10^{-3}] \times [0; 170 \times 10^{-3}]$ m^2. The initial center of the bubble, having an initial diameter of $D = 50 \times 10^{-3}$ m, is located at $x_b = 52.5 \times 10^{-3}$ m, and $y_b = 0$ m. The shock wave is initially positioned at $x_s = 10 \times 10^{-3}$ m and moves to the right towards the bubble with a Mach number $M_a = 1.22$. Flow is then initialized by using the Rankine-Hugoniot relationships, and the corresponding initial conditions [65] on density, streamwise velocity, pressure, and heat capacity ratio are:

$$(\rho_0, u_0, p_0, \gamma) = \begin{cases} (1.66\,\text{kg.m}^{-3},\ 114\,\text{m.s}^{-1},\ 159080\,\text{Pa},\ 1.4\ ) & \text{for } x > x_s, \\ (1.2062\,\text{kg.m}^{-3},\ 0,\ 101325\,\text{Pa},\ 1.4) & \text{in air, for } x \leq x_s, \\ (0.2204\,\text{kg.m}^{-3},\ 0,\ 101325\,\text{Pa},\ 1.6451) & \text{inside the He bubble.} \end{cases} \tag{26}$$

Helium and air are both considered as perfect gases.

Cartesian grids are employed in these simulations. The arrangements for the overlapping grids is presented in figure 21. In the followings, meshes are dimensioned with the parameter $Ncells$ that is the number of grid points along the bubble diameter (D). The patch model is a 6×10^{-3} m side square grid, centered on the initial bubble location, and rotated at $\theta = 30°$ (w.r.t. the horizontal axis) in order to stress the geometrical intersections of the Chimera exchange. Let us note that the single grid configuration is equivalent to the substrate model used in the Chimera case.

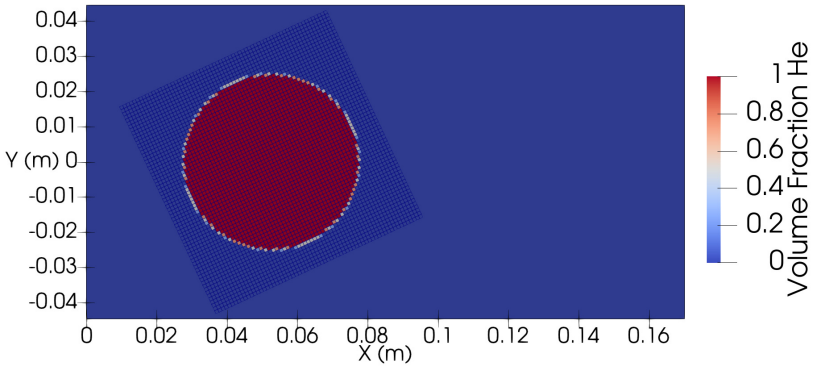

Figure 21: Bubble Shock test case numerical configuration.

Simulations are performed on both the single grid configuration and the overlapping grid case, using a constant CFL number CFL = 0.4, over a dimensionless time of $t^{\star}_{End} = t\ u_0/D = 1.54$. Three grids are considered: $Ncells = 50, 100$, and 200. When the shock wave interacts with the bubble, the bubble is severely deformed and globally moves downstream as we can see in figure 22 where iso-countours of the Helium volume fraction are plotted at two dimensionless time $t^{\star} = 0.24$, and 1.54 for the single grid configuration with $Ncells = 200$. As Helium is less dense than the surrounding Air, the bubble acts as a divergent acoustic lens explaining deformations. In fact, as the gradient of pressure induced by the shock wave is not always aligned with the gradient of density imposed by the Air/Helium interface, vorticity is locally produced by baroclinic effect explaining the deformation and the interface coiling. This present single mesh solution using the finest grid ($Ncells = 200$) fits experimental results from [64]. This grid resolution allows the capture of anti-symmetrical vortices as well as oscillations of the interface on the bubble front. Although vortices are locally produced by baroclinic effect, perfectly anti-symmetrical vortices are produced since the integral of vorticity must stay to zero as no vorticity is present at the initial state. The present single grid simulation allows to account for this physical aspect.

Regarding the Chimera configuration, let us notice that the bubble is only prescribed inside the patch grid and so, does not initially exist in the substrate model. As the patch grid is kept fixed, the bubble moves away from the patch to the substrate during simulations, and at the final time, the bubble is completely located on the right hand side of the substrate mesh and is no longer inside the patch. This allows us to study the robustness of the present Chimera method to deal with a moving two-component interface through the external patch boundary where the local grid spacing abruptly changes. That way, a particular attention will be devoted to examine the field of the Helium volume fraction over time.

In a first step we keep the ratio $\chi = 1$ while grids in both the patch and the substrate models are refined using the three resolutions previously considered $Ncells = 50, 100$, and 200. Iso-

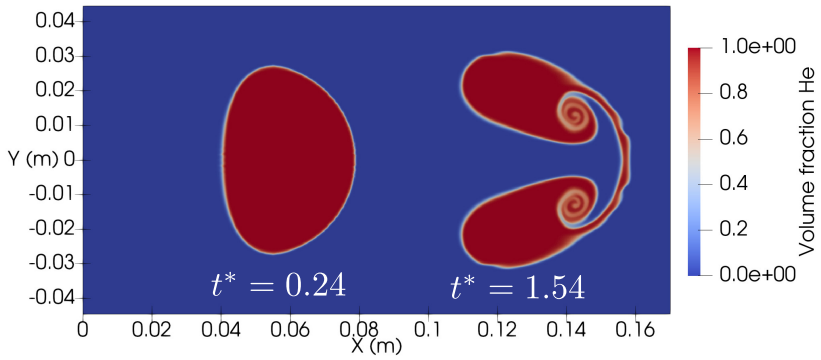

Figure 22: Iso-contours of the Helium volume fraction obtained with a single grid configuration with $Ncells = 200$ at two different dimensionless times $t^\star = 0.24$, and 1.54.

contours of the Helium volume fraction are plotted, at a dimensionless time $t^\star = 1.54$, for both the single grid configuration (Fig. 23), and the overlapping grids (Fig. 24) with $\chi = 1$. Very good agreement is achieved by the present Chimera method on overlapping grids with the same cell ratio ($\chi = 1$), compared to the single grid configuration. The Chimera exchange does not alter the shape of the bubble nor induces sensible perturbations but provides a better description of the bubble curvature due to a more fitted grid. On the finest grid, it is noted that the small symmetry alteration from the Chimera method comes from the symmetry breaking position of the patch. This means that with the coarser grids ($Ncells = 50$ and 100), the Chimera impact is minimal and on the finest grid ($Ncells = 200$), the more adapted grid helps capturing the bubble front but the asymetrical patch grid slighlty breaks the symmetry. We can conclude that the impact of the Chimera exchange on the two-phase interface can help improving the solution with a better fitted grid when $\chi = 1$, fulfilling our requirements.

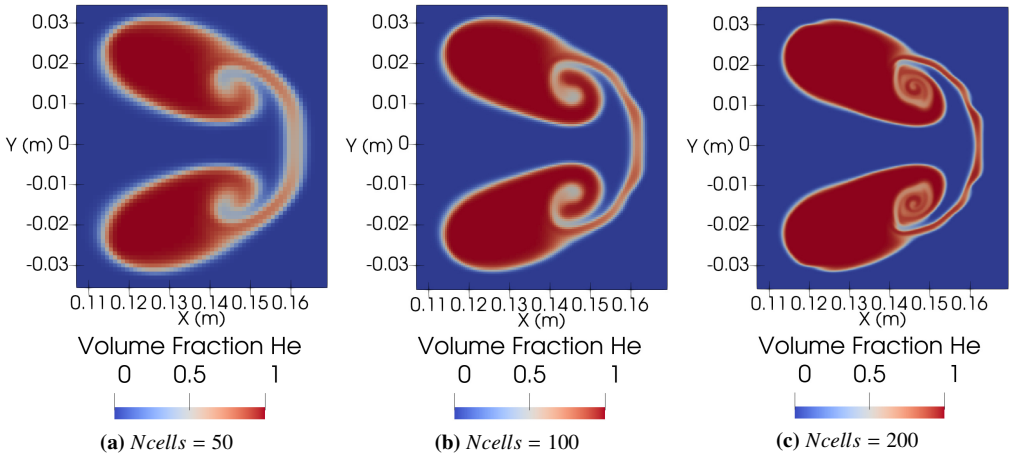

(a) $Ncells = 50$ **(b)** $Ncells = 100$ **(c)** $Ncells = 200$

Figure 23: Helium volume fraction field obtained in the single mesh case at $t^\star = 1.54$, for a number of cells along the bubble diameter of $Ncells = 50$ (on the left), 100 (in the middle), and 200 (on the right).

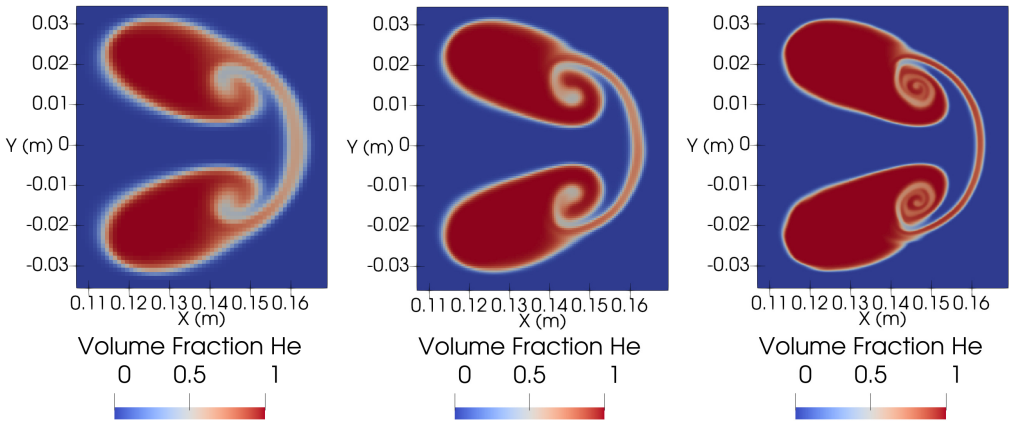

(a) $Ncells = 50$ **(b)** $Ncells = 100$ **(c)** $Ncells = 200$

Figure 24: Helium volume fraction field obtained with the present Chimera method with overlapping grids with the same cell ratio ($\chi = 1$) at $t^\star = 1.54$, for a number of cells along the bubble diameter of $Ncells = 50$ (on the left), 100 (in the middle), and 200 (on the right).

Secondly, we keep the number of grid cells (along the bubble diameter) $Ncells = 50$ constant in the substrate model and increase the ratio $\chi = 1, 2, 4,$ and 8, which respectively correspond to an equivalent mesh refinement of $Ncells = 50, 100, 200,$ and 400 in the patch model. We plot results in figure 25 obtained by using these refinements in the patch, at a dimensionless time $t^\star = 1.54$ after the bubble has crossed the external patch boundary and is fully embedded in the substrate. By using cell ratio greater than 1, we can see that the solution has been improved compared to the single grid solution with the same resolution as the one used in the substrate ($Ncells = 50$). However, although the higher the cell ratio (χ) the better the quality of the final solution, the quality of the solution is mainly impacted by the resolution used in the substrate, and it is obviously hard to recover the quality obtained with the equivalent grid refinement. What it is important to note is that the use of high cell ratios does not introduce numerical artifact but on the contrary improves the quality thanks to the increased grid resolution in the patch. Unlike what Pärt-Enander and Sjögreen [56] observed, we show that refining a patch model in a overlapping grid strategy improves the quality of the solution without any discernable numerical damage on the solution.

4.5. Double Mach Reflection problem

The last problem concerns the emblematic test case of the Double Mach Reflection (DMR) originally proposed by Woodward and Colella [66] as a benchmark for assessing Euler codes. The problem consists in a front shock wave that hits a 30 degree inclined ramp. Going up the ramp, a self similar structure with two triple points develops. A sketch of the flow structure is displayed in figure 26. More detailed explanations of the flow structure can be found in [66, 67]. It is a difficult test case, involving both strong shocks and multiple stems. This case is thus relevant to assess the present Chimera method to deal with complex transient flow structures where multiple shock waves and their interactions creating slip lines occur over time (see Fig. 26). The idea is here to check the ability of the present method to account for multiple discontinuities

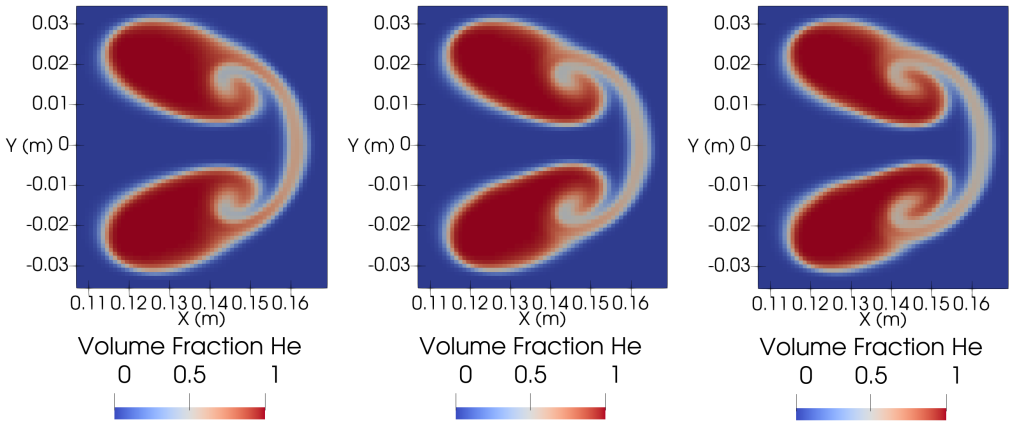

(a) $Ncells = 50, \chi = 1$ **(b)** $Ncells = 50, \chi = 2$ **(c)** $Ncells = 50, \chi = 4$

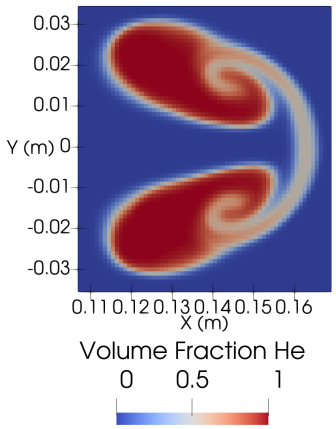

(d) $Ncells = 50, \chi = 8$

Figure 25: Iso-contours of the Helium volume fraction obtained with the present Chimera approach, at a dimensionless time $t^\star = 1.54$, by using several cell ratios ($\chi = 1, 2, 4, 8$).

and their interactions to pass through the external patch boundary where a drastic change of grid spacings can occur.

The numerical configuration of the single mesh case is shown in figure 27a, where the 30° ramp starts at $x_i = 1/6$ m with an overall computational domain length $L_x = 4$ m, and height $L_y = 1$ m. The number of cells in the single mesh configuration is parametrized by $Ncells$ which is the number of cells in the height of the domain. Let us say that the single grid case uses $4Ncells \times Ncells$ grid points in the $(x \times y)$ directions. The shock wave is initially located at $x_s = 1/10$ m. Initial conditions are defined with a driven shock wave moving at a high mach number $M_S = 10$ in Air ($\gamma = 1.4$) initially at rest. Thanks to the Rankine-Hugoniot relationships, initial conditions on primitive variables are:

$$\begin{cases} (\rho, u, v, p)_0 &= (1.4\,\mathrm{kg.m^{-3}}, 0, 0, 1\,\mathrm{Pa}), \\ (\rho, u, v, p)_1 &= (8\,\mathrm{kg.m^{-3}}, 8.25\,\mathrm{m.s^{-1}}, 0, 116.5\,\mathrm{Pa}). \end{cases} \tag{27}$$

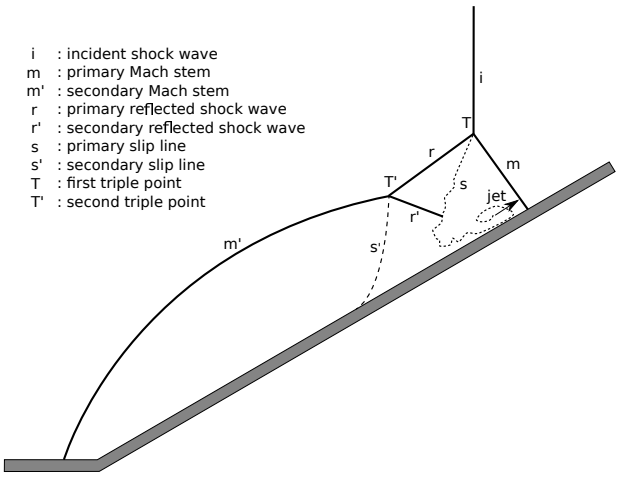

Figure 26: Sketch of the self-similar structure of the Double Mach Reflexion (DMR) problem

As we know in such configuration, the driven shock wave (i, in figure 26) reflects on the wall of the ramp leading to a diffracted bow shock wave (m') that stays ahead of the ramp. This interaction also creates several Mach stems (m, m'). with reflected shock waves (r, r'), triple points (T, T') and subsequent slip lines (s, s'). Issued from the contact discontinuity flow (s), a jet forms along the wall, which is also very difficult to properly predict.

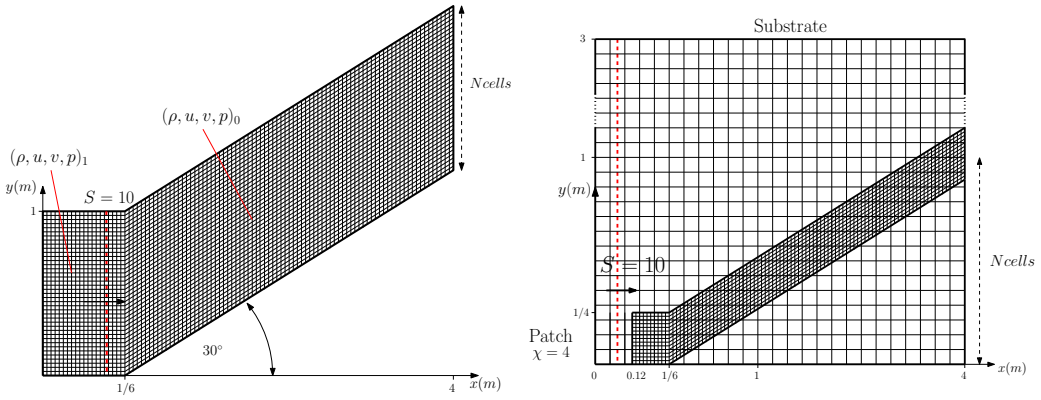

(a) Single mesh

(b) Chimera configuration with $\chi = 4$

Figure 27: Computational domains and initial conditions: configurations of the single mesh case (a), and the Chimera case (b) displayed with a cell ratio $\chi = 4$.

Regarding the Chimera configuration as shown in the figure 27b, the substrate is a standard Cartesian H-grid ($L_x = 4\,\text{m}$ long and $L_y = 3\,\text{m}$ high) configured with the parameter $Ncells$ in order to respect the same grid resolution as the single mesh case. Let us notice that the substrate comprises $Ncells$ grid points over 1 meter. The patch uses the same geometry as the one of the single grid configuration, that is however positioned so that the bottom surface coincides with

that of the substrate. The patch model can be refined using the χ parameter measuring the cell ratio between grid spacings from the substrate and the patch models. As we can see in figure 27b, the driven shock wave is initially located ahead of the patch grid, unlike the original test case of [66]. The dimension of the patch is then chosen so as to allow multiple strong shock waves and the related triple points and slip lines to pass through the external boundary of the patch to study the robustness of the present Chimera method when grid spacings abruptly change. Therefore, the patch extends from $x = 0.12$ m to the end of the substrate, and is $1/4$ m high. This grid configuration has been chosen in order to assess the impact of the proposed Chimera method on flow structures generated inside the patch that cross the overlapping grid interface. The single mesh configuration has then been adapted to be as close as possible to the Chimera configuration.

Simulations are performed on the overlapping grid configuration as well as the single mesh case to allow validation. The CFL number is constant and equal to CFL = 0.4.

At first, we keep the cell ratio between the patch and the substrate at $\chi = 1$ and use $Ncells = 160$ grid points over 1 meter. Results obtained at an equivalent dimensionless time $t^\star = t\,S/L_x = 0.2 + t_0^\star$ (where S is the speed of the driven shock wave and $t_0^\star$ is the theoretical dimensionless time needed for the shock to go from $x_s = 0.1$ m to $x = 1/6$ m) are plotted in figure 28 where the Chimera case (black iso-contour lines) is compared to the single grid configuration (red iso-contour lines). The patch boundary is materialized with the dashed white line.

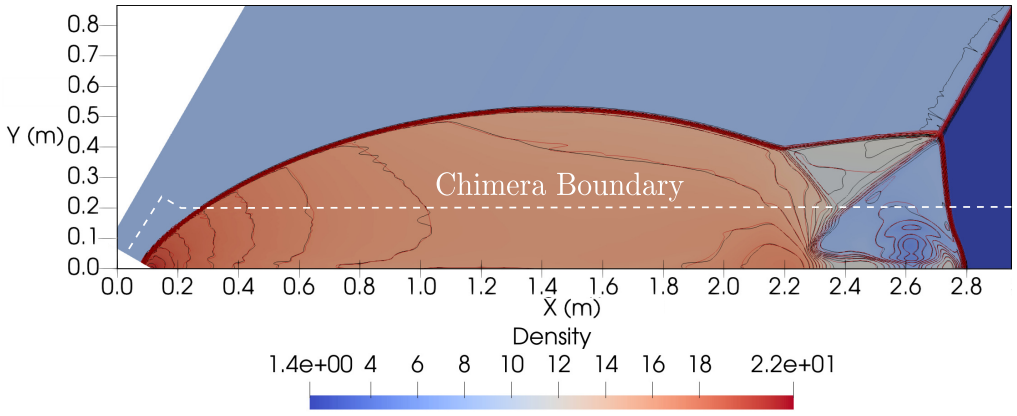

Figure 28: Density contours obtained with the present Chimera approach (black iso-contour lines) compared to the single mesh case (red iso-contour lines) at an equivalent dimensionless time $t^\star = 0.2 + t_0^\star$ for $Ncells = 160$ and $\chi = 1.0$. 30 density contours from $\rho = 1.4$ to 21.4. Dashed white line materializes the patch boundary.

Compared to the single grid configuration, a very good agreement is achieved by the present Chimera method since Mach stems, reflected shock waves as well as slip lines are coincident. The jet located at the end of the ramp is also similarly described with the Chimera method since it is always located inside the patch. These results can also be compared to results from Stone *et al.* [68] (Fig. 16) obtained using a second order accurate scheme in both time and space, that can be taken as reference solutions. Concerning the Chimera case, few oscillations can be observed in the substrate part that may result from solution transfers between overlapping grids that might interfere with acoustic waves. Secondly, we check the influence of the cell ratio parameter (χ). The number of grid cells in the substrate is kept constant and equal to $Ncells = 80$ cells over 1 meter. The cell ratio is varied using three values $\chi = 2, 4$, and 8 which correspond

to an equivalent single mesh resolution respectively using $Ncells = 160,\ 320$, and 640 grid cells over 1 meter. Results on the density contours (black iso-contour lines) obtained with the present Chimera method are presented in figure 29 for $\chi = 2$, Fig. 30 for $\chi = 4$, and Fig. 31 for $\chi = 8$, and compared to their equivalent fine single grid solution (red iso-contour lines) obtained with respectively $Ncells = 160$, 320 and 640. At moderate cell ratio value ($\chi = 2, 4$), the overall comparison is very good, although oscillations present inside the substrate are slightly accentuated when the refinement increases but these oscillations do not seem to interfere with what occurs in the patch. In contrast, flow patterns inside the patch are better predicted as the cell ratio has been increased, mainly the jet that forms at the end of the ramps that has an equivalent description to the equivalent fine single mesh solution. However, when increasing to much the ratio to a high value $\chi = 8$ (Fig. 31), the abrupt change in grid spacing at the external boundary of the patch induces perturbations. As shear layers are likely to develop instabilities, oscillations are mainly visible in the slip line that also alter the jet flow structure.

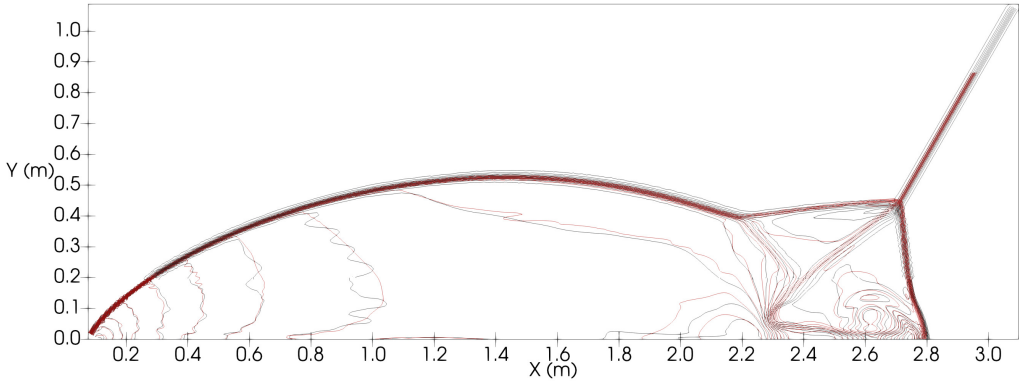

Figure 29: Density contours obtained with the present Chimera approach (black iso-contour lines) by using $Ncells = 80$ cells on the substrate and a cell ratio $\chi = 2$ on the patch, compared to the single mesh case (red iso-contour lines) with $Ncells = 160$, at an equivalent dimensionless time $t^\star = 0.2 + t_0^\star$. 30 density contours from $\rho = 1.4$ to 21.4.

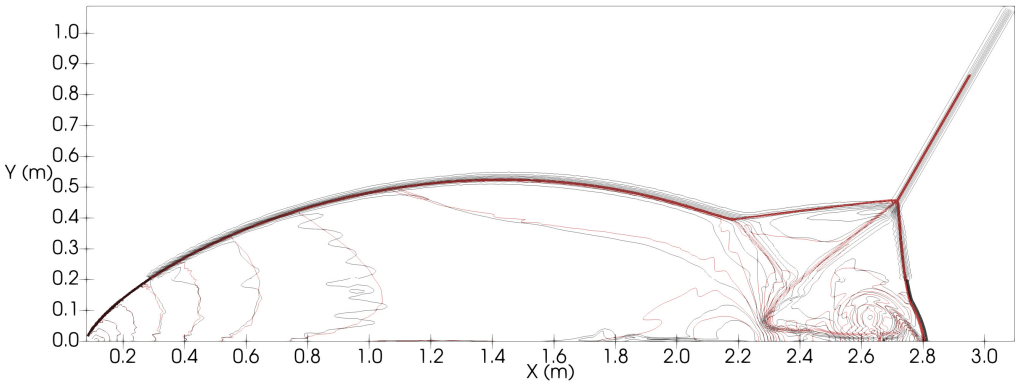

Figure 30: Density contours obtained with the present Chimera approach (black iso-contour lines) by using $Ncells = 80$ cells on the substrate and a cell ratio $\chi = 4$ on the patch, compared to the single mesh case (red iso-contour lines) with $Ncells = 320$, at an equivalent dimensionless time $t^\star = 0.2 + t_0^\star$. 30 density contours from $\rho = 1.4$ to 21.4.

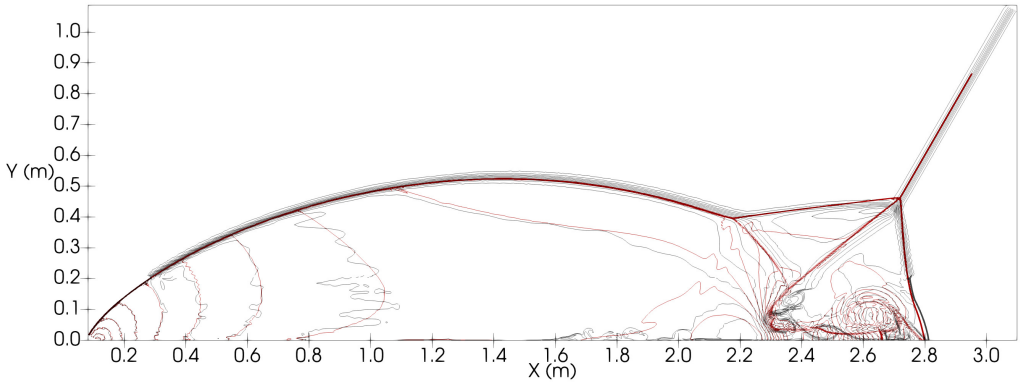

Figure 31: Density contours obtained with the present Chimera approach (black iso-contour lines) by using $Ncells = 80$ cells on the substrate and a cell ratio $\chi = 8$ on the patch, compared to the single mesh case (red iso-contour lines) with $Ncells = 640$, at an equivalent dimensionless time $t^\star = 0.2 + t_0^\star$. 30 density contours from $\rho = 1.4$ to 21.4.

We can conclude that the proposed Chimera method, with reasonable cell ratios, gives good results by increasing the quality of the solution with however useful gains in the CPU time and memory usage compared to a single grid computation. This is confirmed in table 8, where we report the ratios with respect to single grid computations with the equivalent number of cells ($Ncells$) of the CPU time as well as the memory usage. When $\chi = 1$, the ratio is lower than 1 expressing that the Chimera method costs because of a higher number of grid cells, interpolation and transfer of ghost cell solutions. However, compared to single mesh computations with same grid resolutions, once we increase χ, equivalent results are obtained at a much lower cost, mainly coming from the gain in the number of grid points since the time step is equivalent because the grid spacing is the same. Again, even though the present Chimera method is not intended to grid optimization, the method allows significant gains in time and memory without impacting the resulting solution. Nevertheless, when strong waves pass through the patch/substrate interface some numerical actifacts can be recorded when the value of the cell ratio (χ) is too high, at least greater than 4 which imposes an abrupt grid spacing change.

Table 8: Results obtained with the Chimera cases ($Ncells = 80$), compared with their equivalent fine single grid computations.

χ	$Ncells$ EFSM	CPU time ratio	CPU memory ratio
1	80	0.39	0.43
2	160	1.14	1.30
4	320	2.38	2.67
8	640	2.54	3.62

5. Conclusion and open prospects

The present work provides with a numerical strategy which consists of superimposing a local grid (named the patch) onto a global one (namely the substrate). The goal sought after was to superimpose onto the global solution geometrical details accounted in a refined overlapping grid to access to more sophisticated physical aspects, and increase the overall quality of the solution in the region of overlap. We have built an approach based on the Chimera method that is compatible with multi-component flows in order to be adapted to accidental situations involving explosive configurations that can be influenced by geometrical details.

The proposed method relies on data transfers through 2nd-order interpolations using an integral piecewise linear approximation of the solution to update solution in ghost cells that are defined in both the substrate and the patch in a layer edging the interface of the overlapping region. As an explicit time integration is used, ghost cells allow the evaluation of numerical fluxes at cell interfaces close to the overlapping region. To avoid spurious oscillations close to discontinuities in solution reconstruction at cell interfaces as well as in interpolations, a modified version of the finite volume K-Dubois limiter has been proposed to be adapted to the proposed Chimera method since it prevents occurrence of local extrema when high cell size ratios are used between the patch and the substrate. The proposed Chimera method have then been assessed by using five well-known test cases; each test case is chosen to exhibit capabilities and limitations of the method on specific aspects. We have demonstrated with a linear advection of a smooth solution that the second order Chimera reconstruction does not alter the order of convergence of the global solution. The use of high cell ratios on the patch can improve the quality of the global solution although this improvement is however curtailed by the grid resolution used in the global model. A coincident and converged stationary shock, showed that even though the method is not conservative, its impact on conservativity is of an order of magnitude of 0.1% of the inital state which is reasonable for industrial applications. The supersonic flow around a circular cylinder has shown that the proposed Chimera method allows inclusion of a geometrical detail inside a global calculation. The Chimera method favorably affects the final results compared to the single mesh case, and equivalent results are obtained at a much lower computational cost when high cell ratios in the patch are employed because of the gain realized on the number of grid points. The third test case has demonstrated the ability of the proposed Chimera method to account for multi-component flows where a shock wave interacts with a two-fluid interface. Unlike Pärt-Enander and Sjögreen [56], we demonstrated that refining patch cells in an overlapping grid strategy improves the quality of the solution without any discernable numerical damage on the solution. Finally, the last test case, showed that the proposed Chimera method, with reasonable cell ratios ($\chi \leq 4$), improves the quality of the solution compared to a single grid computation, with useful gains in the CPU time and memory usage.

The validation of the method is made on reference two-dimensional cases but the grid intersections are already 3D compatible for industrial applications. The validation of the method on complex 3D cases is in the scope of a future work. In this paper, we only studied the ability of the present Chimera method to deal with fast transient dynamics with wave propagations in compressible flows as well as contact discontinuities usually present in multi-component flows. However, interactions of moving strong discontinuities with flexible structures often occur in accidental configurations involving explosions. Therefore, if one wants to include geometrical details that could influence the Fluid-Structure Interaction (FSI), we must extent the Chimera method to deal with moving deformable structures. In the next future, we will tackle this difficult problem with a special attention devoted to situations where the deformable structure crosses the

boundary of the overlapping grid. Our focus will be on an immersed boundary approach to easily account for fluid structure coupling mainly following the recent work done in [69].

References

[1] J. Park, Y. Cho, S. Kim, J. Lee, Effects of leak rate on LOCA probability of pipes in nuclear power plants, 2014. doi:10.1533/9780081002254.203.

[2] M. Joyce, Nuclear Safety and Regulation, 2018. doi:10.1016/b978-0-08-100962-8.00014-7.

[3] V. Faucher, P. Galon, A. Beccantini, F. Crouzet, F. Debaud, T. Gautier, Hybrid parallel strategy for the simulation of fast transient accidental situations at reactor scale, Annals of Nuclear Energy (2014) to appear. URL: https://hal.archives-ouvertes.fr/hal-01101743. doi:10.1016/j.anucene.2014.07.049.

[4] M. J. Berger, P. Collela, Local adaptive mesh refinement, Journal of Computational Physics (1989) 64–84.

[5] H. Ben Dhia, Problemes mecaniques multi-echelles: La methode Arlequin, Comptes Rendus de l'Academie de Sciences - Serie IIb: Mecanique, Physique, Chimie, Astronomie 326 (1998) 899–904. doi:10.1016/S1251-8069(99)80046-5.

[6] D. Rixen, C. Farhat, M. Géradin, A two-step, two-field hybrid method for the static and dynamic analysis of substructure problems with conforming and non-conforming interfaces, Computer Methods in Applied Mechanics and Engineering 154 (1998) 229 – 264. URL: http://www.sciencedirect.com/science/article/pii/S004578259700128X. doi:https://doi.org/10.1016/S0045-7825(97)00128-X.

[7] C. R. Dohrmann, S. W. Key, M. W. Heinstein, A method for connecting dissimilar finite element meshes in two dimensions, International Journal for Numerical Methods in Engineering 48 (2000) 655–678. doi:https://doi.org/10.1002/(SICI)1097-0207(20000620)48:5<655::AID-NME893>3.0.CO;2-D.

[8] J. Q. Broughton, F. F. Abraham, N. Bernstein, E. Kaxiras, Concurrent coupling of length scales: Methodology and application, Physics Revision B 60 (1999) 2391–2403. URL: https://link.aps.org/doi/10.1103/PhysRevB.60.2391. doi:10.1103/PhysRevB.60.2391.

[9] H. Ben Dhia, Further insights by theoretical investigations of the multiscale Arlequin method, International Journal for Multiscale Computational Engineering 6 (2008) 215–232. doi:10.1615/IntJMultCompEng.v6.i3.30.

[10] O. Jamond, H. Ben Dhia, Incompressibility in the multimodel arlequin framework, International Journal for Numerical Methods in Engineering 94 (2013) 374–399. URL: https://onlinelibrary.wiley.com/doi/abs/10.1002/nme.4454. doi:https://doi.org/10.1002/nme.4454. arXiv:https://onlinelibrary.wiley.com/doi/pdf/10.1002/nme.4454.

[11] A. Fernier, V. Faucher, O. Jamond, Multi-model arlequin approaches for fast transient, fsi-oriented, fluid dynamics with explicit time integration, Computers and Fluids 199 (2020) 104428. URL: http://www.sciencedirect.com/science/article/pii/S0045793020300049. doi:https://doi.org/10.1016/j.compfluid.2020.104428.

[12] J. W. D. Fernandes, A. Barbarulo, H. Ben Dhia, R. A. K. Sanches, A residual-based stabilized finite element formulation for incompressible flow problems in the arlequin framework, Computer Methods in Applied Mechanics and Engineering 370 (2020) 113073. URL: http://www.sciencedirect.com/science/article/pii/S0045782520302577. doi:https://doi.org/10.1016/j.cma.2020.113073.

[13] A. Fernier, V. Faucher, O. Jamond, Multi-model Arlequin method for transient structural dynamics with explicit time integration, International Journal for Numerical Methods in Engineering 112 (2017) 1194–1215. doi:10.1002/nme.5553.

[14] A. Fernier, Multi-model coupling for fluid structure interaction (2019).

[15] J. Steger, J. Benek, A Chimera grid scheme, Advances in Grid Generation (1983) 59–69.

[16] J. A. Benek, A grid-embedding technique, Technical Report (1986).

[17] J. Steger, J. Benek, On the use of composite grid schemes in computational aerodynamics, Computer Methods in Applied Mechanics and Engineering 64 (1987) 301–320.

[18] W. D. Henshaw, Ogen: An overlapping grid generator for Overture, LANL unclassified report (1998) 96–3466.

[19] W. D. Henshaw, D. W. Schwendeman, An adaptive numerical scheme for high-speed reactive flow on overlapping grids, Journal of Computational Physics 191 (2003) 420–447. doi:10.1016/S0021-9991(03)00323-1.

[20] W. D. Henshaw, D. W. Schwendeman, Moving overlapping grids with adaptive mesh refinement for high-speed reactive and non-reactive flow, Journal of Computational Physics 216 (2006) 744–779. doi:10.1016/j.jcp.2006.01.005.

[21] G. Chesshire, W. D. Henshaw, Composite overlapping meshes for the solution of partial differential equations, Journal of Computational Physics 90 (1990) 1–64. doi:10.1016/0021-9991(90)90196-8.

[22] S. E. Sherer, J. N. Scott, High-order compact finite-difference methods on general overset grids, Journal of Computational Physics 210 (2005) 459–496. doi:10.1016/j.jcp.2005.04.017.

[23] R. L. Meakin, Moving body overset grid methods for complete aircraft tilrotor simulations., AIAA paper 3350 (1993).

[24] R. L. Meakin, An efficient means of adaptive refinement within systems of overset grids., AIAA paper 1722 (1995).

[25] N. C. Prewitt, D. M. Belk, W. Shyy, Parallel computing of overset grids for aerodynamic problems with moving objects, Progress in Aerospace Sciences 36 (2000) 117–172.
[26] E. Basso, A. P. Antunes, J. L. F. Azevedo, Chimera simulations of supersonic flows over a complex satellite launcher configuration, Journal of Spacecraft and Rockets 40 (2003) 345–355. doi:10.2514/2.3969.
[27] J. B. Angel, J. W. Banks, W. D. Henshaw, High-order upwind schemes for the wave equation on overlapping grids: Maxwell's equations in second-order form, Journal of Computational Physics 352 (2018) 534–567. doi:10.1016/j.jcp.2017.09.037.
[28] J. Y. Tu, L. Fuchs, Overlapping grids and multigrid methods for three-dimensional unsteady flow calculations in IC engines, International Journal for Numerical Methods in Fluids 15 (1992) 693–714. doi:10.1002/fld.1650150605.
[29] E. R. Elliot, L. Qiu, Y. Yu, R. Fedkiw, Chimera grids for water simulation, Proceedings - SCA 2013: 12th ACM SIGGRAPH / Eurographics Symposium on Computer Animation (2013) 85–94. doi:10.1145/2485895.2485897.
[30] Z. J. Wang, A Fully Conservative Interface Algorithm for Overlapped Grids, Journal of Computational Physics 122 (1995) 96–106.
[31] Z. J. Wang, A conservative interface algorithm for moving Chimera (overlapped) grids, International Journal of Computational Fluid Dynamics 10 (1998) 255–265. doi:10.1080/10618569808961689.
[32] C. Wolf, A chimera simulation method and detached eddy simulation for vortex-airfoil interactions., Ph.D. thesis, Georg-Augus-Universitëxitedat Göttingen, 2011.
[33] T. Aoyama, C. Yang, S. Saito, Numerical analysis of active flap for noise reduction using moving overlapped grid method, Journal of the American Helicopter Society 52 (2007) 189–200. doi:doi:10.4050/JAHS.52.189.
[34] C. Benoit, G. Jeanfaivre, Three-dimensional inviscid isolated rotor calculations using chimera and automatic cartesian partitioning methods, Journal of the American Helicopter Society 48 (2003) 128–138. doi:10.4050/JAHS.48.128.
[35] G. Houzeaux, R. Codina, A Chimera method based on a Dirichlet/Neumann(Robin) coupling for the Navier-Stokes equations, Computer Methods in Applied Mechanics and Engineering 192 (2003) 3343–3377. doi:10.1016/S0045-7825(03)00276-7.
[36] G. Houzeaux, B. Eguzkitza, R. Aubry, H. Owen, M. Vázquez, A Chimera method for the incompressible Navier-Stokes equations, International Journal for Numerical Methods in Fluids 75 (2014) 155–183. doi:10.1002/fld.3886.
[37] K. H. Kao, M. S. Liou, C. Y. Chow, Grid adaptation using chimera composite overlapping meshes., AIAA journal 32 (1994) 942–949.
[38] K. H. Kao, M. S. Liou, Advance in overset grid schemes: From Chimera to DRAGON grids., AIAA journal 33 (1995) 1809–1815.
[39] T. Renaud, M. Costes, S. Péron, Computation of goahead configuration with chimera assembly, Aerospace Science and Technology 19 (2012) 50–57. URL: https://www.sciencedirect.com/science/article/pii/S127096381100109X. doi:https://doi.org/10.1016/j.ast.2011.07.001, gOAHEAD.
[40] B. Landmann, M. Montagnac, A highly automated parallel Chimera method for overset grids based on the implicit hoe cutting technique , International Journal for Numerical Methods in Fluids 66 (2011) 778–804. doi:10.1002/fld.
[41] K. R. Lee, J. H. Park, K. H. Kim, High-order interpolation method for overset grid based on finite volume method, AIAA Journal 49 (2011) 1387–1398. doi:10.2514/1.J050620.
[42] L. Ramírez, C. Foulquié, X. Nogueira, S. Khelladi, J.-C. Chassaing, I. Colominas, New high-resolution-preserving sliding mesh techniques for higher-order finite volume schemes, Computers and Fluids 118 (2015) 114–130. URL: https://www.sciencedirect.com/science/article/pii/S0045793015001917. doi:https://doi.org/10.1016/j.compfluid.2015.06.008.
[43] L. Ramírez, X. Nogueira, P. Ouro, F. Navarrina, S. Khelladi, I. Colominas, A higher-order Chimera method for finite volume schemes, Archives of Computational Methods in Engineering 25 (2018) 691–706. doi:10.1007/s11831-017-9213-8.
[44] P. Gamnitzer, W. A. Wall, An ALE-Chimera method for large deformation fluid structure interaction, Proceedings of the European Conference on Computational Fluid Dynamics, ECCOMAS CFD, The Netherlands, TU Delft (2006) 1–14. URL: http://proceedings.fyper.com/eccomascfd2006/documents/550.pdf.
[45] S. B. Pope, Turbulent Flows, Cambridge University Press, 2000. doi:10.1017/CBO9780511840531.
[46] G. Allaire, S. Clerc, S. Kokh, A five-equation model for the simulation of interfaces between compressible fluids, Journal of Computational Physics 181 (2002) 577–616. doi:10.1006/jcph.2002.7143.
[47] B. Van Leer, Towards the ultimate conservative difference scheme. IV. A new approach to numerical convection, Journal of Computational Physics 23 (1977) 276–299. doi:10.1016/0021-9991(77)90095-X.
[48] B. Van Leer, Towards the ultimate conservative difference scheme iii. upstream-centered finite-difference schemes for ideal compressible flow, Journal of Computational Physics 23 (1977) 263–275. URL: https://

www.sciencedirect.com/science/article/pii/0021999177900948. doi:https://doi.org/10.1016/0021-9991(77)90094-8.

[49] B. van Leer, Towards the ultimate conservative difference scheme. v. a second-order sequel to godunov's method, Journal of Computational Physics 32 (1979) 101–136. URL: https://www.sciencedirect.com/science/article/pii/0021999179901451. doi:https://doi.org/10.1016/0021-9991(79)90145-1.

[50] E. F. Toro, Riemann Solvers and Numerical Methods for Fluid Dynamics, 2009. doi:10.1007/b79761.

[51] D. Solyga, P. Galon, Introduction d'une nouvelle méthode de reconstruction du second ordre en temps et en espace basée sur les variables primitives, Unpublished (2015). doi:10.13140/rg.2.1.1471.0888.

[52] D. Mavriplis, 2003: Revisiting the least-squares procedure for gradient reconstruction on unstructured meshes, 16th AIAA Computational Fluid Dynamics Conference (2003). doi:10.2514/6.2003-3986.

[53] E. Johnsen, T. Colonius, Implementation of weno schemes in compressible multicomponent flow problems, Journal of Computational Physics 219 (2006) 715–732. URL: https://www.sciencedirect.com/science/article/pii/S0021999106002014. doi:https://doi.org/10.1016/j.jcp.2006.04.018.

[54] D. Drikakis, J. Majewski, J. Rokicki, J. Óltak, Investigation of blending-function-based overlapping-grid technique for compressible flows, Computer Methods in Applied Mechanics and Engineering 190 (2001) 5173–5195. doi:10.1016/S0045-7825(00)00373-X.

[55] H. Versteeg, W. Malalasekera, An Introduction to Computational Fluid Dynamics: The Finite Volume Method, Pearson Education Limited, 2007. URL: https://books.google.fr/books?id=RvBZ-UMpGzIC.

[56] E. Pärt-Enander, B. Sjögreen, Conservative and non-conservative interpolation between overlapping grids for finite volume solutions of hyperbolic problems, Computers and Fluids 23 (1994) 551–574.

[57] T. Barth, D. Jespersen, The design and application of upwind schemes on unstructured meshes (1989). URL: https://arc.aiaa.org/doi/abs/10.2514/6.1989-366. doi:10.2514/6.1989-366. arXiv:https://arc.aiaa.org/doi/pdf/10.2514/6.1989-366.

[58] F. Daude, P. Galon, Z. Gao, E. Blaud, Numerical experiments using a HLLC-type scheme with ALE formulation for compressible two-phase flows five-equation models with phase transition, Computers and Fluids 94 (2014) 112–138. URL: http://dx.doi.org/10.1016/j.compfluid.2014.02.008. doi:10.1016/j.compfluid.2014.02.008.

[59] D. Iampietro, F. Daude, P. Galon, A low-diffusion self-adaptive flux-vector splitting approach for compressible flows, Computers and Fluids 206 (2020) 104586. URL: https://doi.org/10.1016/j.compfluid.2020.104586. doi:10.1016/j.compfluid.2020.104586.

[60] R. Liska, B. Wendroff, Comparison of several difference schemes for the euler equations in 1d and 2d, in: T. Y. Hou, E. Tadmor (Eds.), Hyperbolic Problems: Theory, Numerics, Applications, Springer Berlin Heidelberg, Berlin, Heidelberg, 2003, pp. 831–840.

[61] Z. Wang, N. Hariharan, R. Chen, Recent development on the conservation property of chimera, International Journal of Computational Fluid Dynamics 15 (2001) 265–278. doi:10.1080/10618560108970033.

[62] J. Sinclair, X. Cui, A theorical approximation of the shock standoff distance for supersonic flows around a circular cylinder., Physics of Fluids 29 (2017).

[63] J.-F. Haas, B. Sturtevant, Interaction of weak shock waves with cylindrical and spherical gas inhomogeneities., J. Fluid Mech. (1987) 41–76.

[64] G. Layes, G. Jourdan, L. Houas, Distortion of a spherical gaseous interface accelerated by a plane shock wave, Phys. Rev. Lett. (2003).

[65] M. Capuano, C. Bogey, P. Spelt, Simulations of viscous and compressible gas-gas flows using high-order finite difference schemes., Journal of Computational Physics (2018) 56–81.

[66] P. Woodward, P. Collela, The numerical simulation of two-dimensional fluid flow with strong shocks, Journal of Computational Physics (1984) 115–173.

[67] U. S. Vevek, B. Zang, T. H. New, On alternative setups of the double Mach reflection problem, Journal of Scientific Computing (2018).

[68] J. M. Stone, T. A. Gardiner, P. Teuben, J. F. Hawley, J. B. Simon, Athena: A new code for astrophysical MHD, The Astrophysical Journal Supplement Series 178 (2008) 137–177. URL: https://doi.org/10.1086/588755. doi:10.1086/588755.

[69] O. Jamond, A. Beccantini, An embedded boundary method for an inviscid compressible flow coupled to deformable thin structures: The mediating body method, International Journal for Numerical Methods in Engineering 119 (2019) 305–333. URL: https://onlinelibrary.wiley.com/doi/abs/10.1002/nme.6051. doi:https://doi.org/10.1002/nme.6051. arXiv:https://onlinelibrary.wiley.com/doi/pdf/10.1002/nme.6051.